

Linear-Response and Nonlinear-Response Formulations of the Instantaneous Marcus Theory for Nonequilibrium Photoinduced Charge Transfer

Dominikus Brian and Xiang Sun*



Cite This: *J. Chem. Theory Comput.* 2021, 17, 2065–2079



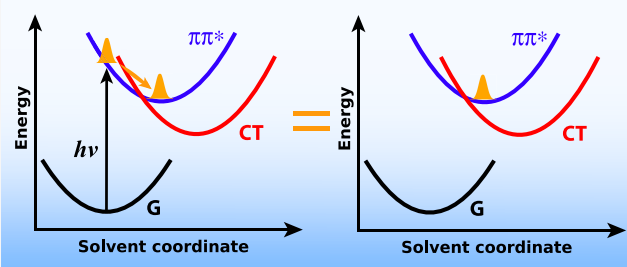
Read Online

ACCESS |

Metrics & More

Article Recommendations

ABSTRACT: Instantaneous Marcus theory (IMT) offers a way for capturing the time-dependent charge transfer (CT) rate coefficient in nonequilibrium photoinduced CT processes, where the system was photoexcited from its equilibrated ground state vertically to the excitonic state, followed by an electronic transition to the CT state. As derived from the linearized semiclassical nonequilibrium Fermi's golden rule (LSC NE-FGR), the original IMT requires expensive all-atom nonequilibrium molecular dynamics (NEMD) simulations. In this work, we propose computationally efficient linear-response and nonlinear-response formulations for IMT rate calculations, which only require equilibrium molecular dynamics simulations. The linear- and nonlinear-response IMT methods were tested to predict the transient behavior in the photoinduced CT dynamics of the carotenoid–porphyrin–C₆₀ molecular triad solvated in explicit tetrahydrofuran. Our result demonstrated that the nonlinear-response IMT is in excellent agreement with the benchmark NEMD for all cases investigated here, whereas the linear-response IMT predicts the correct trend for all cases but overestimates the transient CT rate in one case involving a significant nonequilibrium relaxation. This mild breakdown of linear-response IMT is due to neglecting the higher-order terms in the exact nonlinear-response IMT. Taking advantage of time translational symmetry, the linear- and nonlinear-response approaches were demonstrated to be able to reduce the computational cost by 80% and 60% compared with NEMD simulations, respectively. Thus, we highly recommend the readily applicable and accurate nonlinear-response IMT approach for simulating nonequilibrium CT processes in complex molecular systems in the condensed phase.



1. INTRODUCTION

Photoinduced charge transfer (CT) is a ubiquitous fundamental process that is at the core of natural and artificial photosynthesis as well as organic photovoltaic solar cells.^{1–13} Accurate modeling of photoinduced CT dynamics is key for grasping the molecular mechanism that underlies the governing principle of energy conversion and developing rational design principles toward optimizing energy conversion performance.^{14–17} Despite the fact that several quantum dynamical theories have been proposed for dealing with CT dynamics in single molecules in the gas phase,^{18–23} fully quantum-mechanical CT dynamics for condensed-phase systems still remains challenging.

That being said, the classic Marcus theory has been employed extensively for computing CT rate constants in a variety of complex systems in the condensed phase.^{24–26} The popularity of Marcus theory may be traced back to the fact that the Marcus donor-to-acceptor CT rate constant is expressed in terms of only three parameters: the donor–acceptor electronic coupling (Γ_{DA}), the reaction free energy (ΔE), and the reorganization energy (E_r) as in eq 1:

$$k_{D \rightarrow A}^M = \frac{|\Gamma_{DA}|^2}{\hbar} \sqrt{\frac{\pi}{k_B T E_r}} \exp\left[-\frac{(\Delta E + E_r)^2}{4k_B T E_r}\right] \quad (1)$$

From the intuitive parabolic picture, Marcus theory offers a straightforward approach for understanding and predicting the trend of CT rate constant with an increasing thermodynamic driving force, leading to the famous turnover from the normal regime into the inverted regime.

However, Marcus theory cannot account for the effects caused by the nonequilibrium nature of the initial preparation, as in most photoinduced CT process, the initial state of the system is usually at thermal equilibrium on the ground state, but Marcus theory is based on the assumptions that the nuclear

Received: December 2, 2020

Published: March 9, 2021



degrees of freedom (DOF) start out at thermal equilibrium on the donor electronic potential energy surface (PES).²⁷ Thus, the instantaneous CT rate coefficient may deviate from the CT Marcus rate constant because of the nuclear structural relaxation on the donor PES following a vertical photoexcitation from thermally equilibrated ground state.^{28–31} Such transient nonequilibrium effects are expected to be significant when the time scale of nuclear relaxation on the excited state is comparable to the time scale of the electronic transition.

In contrast, the recently proposed instantaneous Marcus theory (IMT)³² is designed to account for the effects due to the nonequilibrium initial preparation, where the time-dependent transient CT rate coefficient is given by a Marcus-like expression with explicitly time-dependent donor–acceptor energy gap average and its standard deviation, or equivalently with time-dependent reaction free energy and reorganization energy. This time-dependent IMT expression inherits the simplicity of Marcus theory and, therefore, is easy to apply to condensed-phase systems offering time-dependent transient CT rates that go beyond a single kinetic Marcus CT rate constant.

The formulation of IMT can be derived from taking the classical limit of the linearized semiclassical (LSC) non-equilibrium Fermi's golden rule (NE-FGR).^{31–33} Here, NE-FGR is a quantum-mechanical perturbative approach for obtaining a time-dependent CT rate coefficient with arbitrary nonequilibrium nuclear initial conditions,²⁸ and its LSC approximation allows one to calculate the CT rate coefficient of condensed-phase systems governed by generally anharmonic force fields.^{31,33} For example, LSC NE-FGR has been recently demonstrated in the photoinduced CT in the carotenoid–porphyrin–C₆₀ (CPC₆₀) molecular triad^{34–39} dissolved in an explicit tetrahydrofuran (THF) solvent whose interactions are described by all-atom anharmonic force fields,^{40–44} and IMT was shown to reproduce the LSC NE-FGR time-dependent CT rate remarkably well.³² Taking the nonequilibrium nature of initial preparation into account would dramatically change the photoinduced CT dynamics, which exhibits a significant difference from the predictions made by using a Marcus theory rate constant.³² It is noted that the conditions under which IMT is expected to be accurate are when (1) the nuclear DOF are classical, (2) the nuclear motion occurs on a time scale slower than the electronic dephasing time, and (3) the distribution of the donor–acceptor energy gap is time-dependent Gaussian.

In practice, both LSC NE-FGR and IMT expressions require nonequilibrium molecular dynamics (NEMD) simulations on the donor PES with initial nuclear conditions sampled on the equilibrated ground PES.³² For realistic organic photovoltaic molecules dissolved in the condensed phase including typically tens or hundreds of thousand of atoms, all-atom NEMD simulation of tens of thousands of trajectories is computationally expensive. It is thus desirable to develop a more efficient computational approach that can bypass the expensive NEMD simulation and still provide a quantitative instantaneous CT rate coefficient.

In this paper, we develop a practical and cost-effective computational approach to IMT for nonequilibrium photoinduced CT that only requires equilibrium molecular dynamics (MD) simulations. The underlying basis for our formalism was the framework of the linear-response theory of statistical mechanics, which relates the nonequilibrium relaxation with fluctuations in the equilibrium state.^{45–50} For example, in a

time-dependent fluorescence Stokes shift measurement of solvation dynamics, the nonequilibrium relaxation of the excited–ground energy gap ΔV can be expressed by

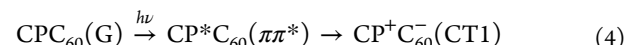
$$S_{\Delta V}(t) = \frac{\overline{\Delta V(t)} - \overline{\Delta V(\infty)}}{\overline{\Delta V(0)} - \overline{\Delta V(\infty)}} \quad (2)$$

where the overbars denote a nonequilibrium average with initial conditions sampled on the ground state and dynamics evolved on the excited state. The linear-response theory dictates that the nonequilibrium relaxation $S(t)$ is equivalent to an equilibrium time correlation function of the fluctuation of the energy gap $\delta\Delta V = \Delta V - \langle \Delta V \rangle_{e/g}$:

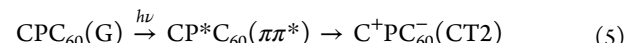
$$C_{\Delta V}(t) = \frac{\langle \delta\Delta V(t)\delta\Delta V(0) \rangle_{e/g}}{\langle (\delta\Delta V)^2 \rangle_{e/g}} \quad (3)$$

where $\langle \cdot \rangle_{e/g}$ denotes an ensemble average of equilibrated excited or ground states.⁴⁵ This relation is remarkable in that if the linear-response theory is valid, then the nonequilibrium relaxation can be calculated from only equilibrium simulations. The linear-response theory has been found to hold for most processes in liquids with only a few breakdown cases where the energy dissipation mechanism is severely altered by some very unique molecular features;^{51–58} for example, a high-speed rotating CN solute kicks the nearby solvents far away, creating a bubble that leads to a very slow rotational relaxation.^{52,53} Also, the ΔV does not have to be small for the linear-response theory to work, a more general version of the linear-response theory assumes only Gaussian statistics of ΔV ,^{45,59–62} which makes it widely applicable in many condensed-phase ultrafast spectroscopies for solvation dynamics.^{45,63–69}

Thus, we propose to develop linear- and nonlinear-response approaches for constructing IMT parameters such that the dynamical information can be calculated with only equilibrium molecular dynamics simulations to reduce the computational overhead in IMT calculation. We test these methods' applicabilities within the context of the photoinduced CT in the CPC₆₀ triad in an explicit THF solvent, which is a complex molecular system described by all-atom anharmonic interactions.^{42,44} In the photoinduced CT processes, the triad is initially in equilibrium on the ground (G) state, CPC₆₀, before being vertically photoexcited to the P-localized excitonic $\pi\pi^*$ state, CP*^{*}C₆₀. The impulsive photoexcitation is then followed by a nonradiative transition to the excited P-to-C₆₀ CT state, CP⁺C₆₀⁻, which is denoted as CT1



or to the excited C-to-C₆₀ charge separated state, C⁺PC₆₀⁻, which is denoted as CT2



A schematic presentation of these CT processes in two characteristic triad conformations (bent and linear) is provided in Figure 1.

From our previous NEMD study, the nonequilibrium donor–acceptor energy gap follows a time-dependent Gaussian distribution, which satisfies the assumption of IMT and also the linear-response theory.³² Also, our LSC NE-FGR and IMT calculations show that taking nonequilibrium initial preparation into account would enhance the transient CT rate of the porphyrin-to-C₆₀ process dramatically (about 40 times), and it originates from the solvent structural relaxation after

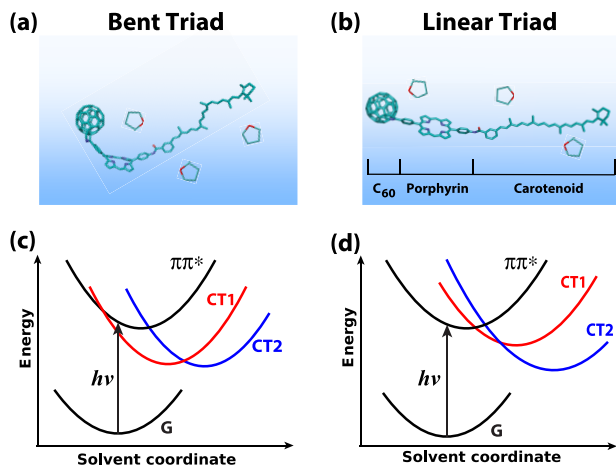


Figure 1. Schematic representations of two characteristic conformations of the carotenoid–porphyrin– C_{60} (CPC_{60}) molecular triad solvated in explicit tetrahydrofuran (THF): the bent triad conformation (a) and the linear triad conformation (b). Potential energy surfaces for different nonequilibrium charge transfer processes in the bent triad conformation (c) and in the linear triad conformation (d): after a vertical photoexcitation from the ground (G) state to the donor (CP^*C_{60} , $\pi\pi^*$) state, there can be donor-to-acceptor nonradiative electronic transitions from $\pi\pi^*$ state to the porphyrin-to- C_{60} CT state, $CP^+C_{60}^-$ (CT1), or from $\pi\pi^*$ state to the carotenoid-to- C_{60} charge separated state, $C^+PC_{60}^-$ (CT2).

photoexcitation from ground state, since freezing the intramolecular DOF in the triad does not change the transient CT rates.³² It is noted that the nuclear motion in this solvated triad solution does not show significant nuclear quantum effects since it does not involve light particles like hydrogen and happens at room temperature, which was supported by our recent study of mapping the all-atom Hamiltonians onto spin-boson models showing very small nuclear quantum effects.⁷⁰

The remainder of this paper is organized as follows. The instantaneous Marcus theory is briefly summarized and the linear- and nonlinear-response formulations for IMT are presented in **Section 2**. The all-atom anharmonic model for CPC_{60} molecular triad dissolved in liquid THF and MD simulation techniques are described in **Section 3**. Results are reported in **Section 4**. Concluding remarks are provided in **Section 5**. The derivation of the quadratic-response formulas for IMT is detailed in **Appendix A**.

2. THEORY

2.1. Instantaneous Marcus Theory from the Non-equilibrium Fermi's Golden Rule. Consider a two-state system with the overall Hamiltonian $\hat{H} = \hat{H}_D|D\rangle\langle D| + \hat{H}_A|A\rangle\langle A| + \Gamma_{DA}(|D\rangle\langle A| + |A\rangle\langle D|)$. Here, $|D\rangle$ and $|A\rangle$ represent the diabatic donor and acceptor electronic states, respectively, $\hat{H}_{D/A}$ are the corresponding nuclear Hamiltonians, $\hat{H}_{D/A} = \hat{\mathbf{P}}^2/2 + V_{D/A}(\hat{\mathbf{R}})$, where $\mathbf{R} = (\hat{R}_1, \dots, \hat{R}_N)$ and $\hat{\mathbf{P}} = (\hat{P}_1, \dots, \hat{P}_N)$ are the mass-weighted nuclear coordinates and momenta, $V_{D/A}(\hat{\mathbf{R}})$ are the donor/acceptor PESs, and Γ_{DA} is the electronic coupling coefficient.

Assuming that the system starts out at the donor electronic state with the initial nuclear DOF described by the ground-state nuclear density operator $\hat{\rho}_G = e^{-\beta\hat{H}_G}/\text{Tr}_n[e^{-\beta\hat{H}_G}]$, where $\hat{H}_G = \hat{\mathbf{P}}^2/2 + V_G(\hat{\mathbf{R}})$ is the ground state nuclear Hamiltonian, $V_G(\hat{\mathbf{R}})$ is the ground PES, $\beta = 1/k_B T$ is the inverse

temperature, and $\text{Tr}_{n/e}(\cdot)$ denotes trace over the nuclear/electronic Hilbert space, the donor-state population $P_D(t)$ is given by

$$P_D(t) = \text{Tr}_n \text{Tr}_e [e^{-i\hat{H}_D t/\hbar} \hat{\rho}_G e^{i\hat{H}_D t/\hbar} |D\rangle\langle D|] \quad (6)$$

Applying the second-order perturbation theory, the NE-FGR donor-state population can be written as²⁸

$$P_D(t) \approx \exp \left[- \int_0^t dt' k(t') \right] \quad (7)$$

where the *time-dependent rate coefficient* is defined as

$$k(t) = \frac{2}{\hbar^2} \text{Re} \int_0^t d\tau C(t, \tau) \quad (8)$$

Here

$$C(t, \tau) = |\Gamma_{DA}|^2 \text{Tr}_n [e^{-i\hat{H}_D t/\hbar} \hat{\rho}_G e^{i\hat{H}_D t/\hbar} e^{-i\hat{H}_A \tau/\hbar} e^{i\hat{H}_D \tau/\hbar}] \quad (9)$$

For a detailed discussion of the LSC approximation of eq 9, as well as the progression of approximations that can be derived from it, the reader is referred to ref 31.

The instantaneous Marcus theory (IMT) expression of $k(t)$ can be derived from the “C-0” level of approximation for the NE-FGR,^{31,32} which corresponds to classical initial sampling:

$$\begin{aligned} k^{C-0}(t) &= \frac{2}{\hbar^2} |\Gamma_{DA}|^2 \text{Re} \int_0^t d\tau \int d\mathbf{R}_0 d\mathbf{P}_0 \times \rho_G(\mathbf{R}_0, \mathbf{P}_0) \\ &\quad \exp \left[\frac{i}{\hbar} U(\mathbf{R}_t^D) \tau \right] \\ &= \frac{2}{\hbar^2} |\Gamma_{DA}|^2 \text{Re} \int_0^t d\tau \langle e^{iU_t \tau/\hbar} \rangle \\ &= \frac{2}{\hbar^2} |\Gamma_{DA}|^2 \text{Re} \int_0^\infty d\tau \langle e^{iU_t \tau/\hbar} \rangle \\ &= \frac{1}{\hbar^2} |\Gamma_{DA}|^2 \left\langle \int_{-\infty}^\infty d\tau e^{iU_t \tau/\hbar} \right\rangle \\ &= \frac{2\pi}{\hbar} |\Gamma_{DA}|^2 \langle \delta(U_t) \rangle \end{aligned} \quad (10)$$

Here, $\rho_G(\mathbf{R}_0, \mathbf{P}_0)$ is the phase-space density that corresponds to the classical limit of $\hat{\rho}_G$, $U(\mathbf{R}) = V_D(\mathbf{R}) - V_A(\mathbf{R})$ is the donor–acceptor potential energy gap, and \mathbf{R}_t^D is the nuclear configuration at time t , obtained via classical dynamics on the donor PES, starting with $(\mathbf{R}_0, \mathbf{P}_0)$ as the initial conditions. In the remainder of the paper, angular brackets without subscript denotes ensemble average over the donor state. The third equal sign in eq 10 is achieved by assuming the lifetime of the integrand $\langle e^{iU_t \tau/\hbar} \rangle$, denoted as τ_c , is much shorter than the time scale of nuclear relaxation, i.e. $t > \tau_c$ ($\tau_c \sim 20$ fs in this case); then we can change the τ integration upper limit to infinity. As a result, the CT rate coefficient is proportional to $\langle \delta(U_t) \rangle$, which is the probability for $U_t = 0$. If we further assume the instantaneous distribution of U_t is Gaussian with a time-dependent mean \bar{U}_t and the corresponding variance $\sigma_t^2 = \bar{U}_t^2 - (\bar{U}_t)^2$ at time t after the photoexcitation

$$\text{Prob}(U_t) = \frac{1}{\sqrt{2\pi\sigma_t^2}} \exp \left[-\frac{(U_t - \bar{U}_t)^2}{2\sigma_t^2} \right] \quad (11)$$

then the IMT CT rate coefficient is given by the following Marcus-like expression:³²

$$k^{\text{IMT}}(t) = \frac{|\Gamma_{DA}|^2}{\hbar} \sqrt{\frac{2\pi}{\sigma_t^2}} \exp\left[-\frac{(\overline{U}_t)^2}{2\sigma_t^2}\right] \quad (12)$$

Here, \overline{U}_t and σ_t can be calculated using NEMD by averaging over many nonequilibrium trajectories that start out with the nuclear DOF sampled from equilibrated ground state, and the subsequent dynamics is propagated on the donor PES. The IMT CT rate coefficient $k^{\text{IMT}}(t)$ can also be expressed equivalently in terms of time-dependent ΔE and E_r :

$$E_r(t) = \frac{\sigma_t^2}{2k_B T} = -\Delta E(t) - \overline{U}_t \quad (13)$$

The conditions under which the IMT expression is reasonably accurate are (1) the nuclear DOF are classical, (2) the nuclear motion occurs on a time scale slower than the electronic dephasing time, i.e. $t > \tau_\sigma$ and (3) the distribution of U_t is time-dependent Gaussian.

Assuming that the initial nuclear DOF are sampled from equilibrated donor state $\hat{\rho}_D = e^{-\beta\hat{H}_D}/\text{Tr}_n[e^{-\beta\hat{H}_D}]$ and the donor-to-acceptor transition happens on a time scale longer than the lifetime of

$$C(\tau) = |\Gamma_{DA}|^2 \text{Tr}_n[\hat{\rho}_D e^{-i\hat{H}_A\tau/\hbar} e^{i\hat{H}_D\tau/\hbar}] \quad (14)$$

that $C(t, \tau)$ reduces to, then leads to $P_D(t) = \exp(-k_{D \rightarrow A} t)$, where $k_{D \rightarrow A}$ is the equilibrium Fermi's golden rule (E-FGR) CT rate constant given by²⁷

$$k_{D \rightarrow A} = \frac{2}{\hbar^2} \text{Re} \int_0^\infty d\tau C(\tau) \quad (15)$$

which will reduce to the Marcus rate constant in eq 1 if taking the classical limit, the short-time limit, and assuming Gaussian distribution in the energy gap. It should be noted that the time-dependent rate coefficient, $k(t)$, replaces the time-independent rate constant, $k_{D \rightarrow A}$, when the nuclear DOF start out at a nonequilibrium initial state, and when the system is fully relaxed to equilibrium on the donor state, $k(t)$ should asymptotically approach $k_{D \rightarrow A}$.^{31,32} Accounting for this effect is important when $k(t)$ and $k_{D \rightarrow A}$ are significantly different and the time scale for reaching thermal equilibrium on the donor PES is comparable to or longer than the time scales of CT, $\sim k_{D \rightarrow A}^{-1}$.

2.2. Linear- and Nonlinear-Response Formulations for IMT.

In this section, we present the classical linear-response (LR) and nonlinear-response (NLR) theories for IMT. In the IMT expression in eq 12, there are two time-dependent quantities, the average donor–acceptor energy gap \overline{U}_t and its corresponding variance σ_t^2 , and both are defined as the nonequilibrium average with the initial condition prepared on the equilibrated ground state and the subsequent dynamics is propagated on the donor state.

Without loosing generality, we denote our donor–acceptor energy gap observable as $A(\mathbf{X})$ where $\mathbf{X} = (\mathbf{R}, \mathbf{P})$ is phase space point and the energy difference between the excited (donor) state and the ground state as $\Delta V(\mathbf{X})$. First of all, we define the time-dependent nonequilibrium average

$$\overline{A(t)} \equiv \frac{\int d\mathbf{X}_0 e^{t\mathcal{L}_D} A(\mathbf{X}_0) e^{-\beta H_G(\mathbf{X}_0)}}{\int d\mathbf{X}_0 e^{-\beta H_G(\mathbf{X}_0)}} \quad (16)$$

$$\begin{aligned} &= \frac{\int d\mathbf{X}_0 A(t) e^{\beta \Delta V(\mathbf{X}_0)} e^{-\beta H_D(\mathbf{X}_0)}}{\int d\mathbf{X}_0 e^{\beta \Delta V(\mathbf{X}_0)} e^{-\beta H_D(\mathbf{X}_0)}} \\ &= \frac{\langle A(t) e^{\beta \Delta V(0)} \rangle}{\langle e^{\beta \Delta V} \rangle} \end{aligned} \quad (17)$$

where $\mathbf{X}_0 = (\mathbf{R}_0, \mathbf{P}_0)$ is the initial phase-space point, $\mathcal{L}_D = -\{H_D, \cdot\}$ is the classical Liouville operator that propagates the system according to the donor state Hamiltonian H_D as in $e^{t\mathcal{L}_D} A(\mathbf{X}_0) = A(\mathbf{X}_t) = A(t)$, and $\langle \cdot \rangle$ is the equilibrium average on the donor state. Also, we use simplified notation here for dynamical variable that is a function of phase space point at a given time, such as $\Delta V(0) = \Delta V(\mathbf{X}_0)$. If we define $\delta A = A - \langle A \rangle$ as the fluctuations about its equilibrium average, eq 17 can be written as⁶⁸

$$\begin{aligned} \overline{A(t)} &= \frac{\langle A(t) e^{\beta \delta \Delta V(0)} \rangle}{\langle e^{\beta \delta \Delta V} \rangle} = \frac{\langle \delta A(t) e^{\beta \delta \Delta V(0)} \rangle}{\langle e^{\beta \delta \Delta V} \rangle} + \langle A \rangle \\ &= C_1^{\text{NL}}(t) + \langle A \rangle \end{aligned} \quad (18)$$

where the first-order nonlinear-response cross time correlation function (TCF) is given by

$$C_1^{\text{NL}}(t) = \frac{\langle \delta A(t) e^{\beta \delta \Delta V(0)} \rangle}{\langle e^{\beta \delta \Delta V} \rangle} \quad (19)$$

The nonequilibrium variance of observable A at time t after the photoexcitation is defined as follows

$$\sigma_t^2 = \overline{[A(t) - \overline{A(t)}]^2} = \overline{A^2(t)} - [\overline{A(t)}]^2 \quad (20)$$

where

$$\overline{A^2(t)} = \frac{\langle \delta A^2(t) e^{\beta \delta \Delta V(0)} \rangle}{\langle e^{\beta \delta \Delta V} \rangle} + \langle A^2 \rangle \quad (21)$$

with $\delta A^2(t) = A^2(t) - \langle A^2 \rangle$. Insert eq 18 and eq 21 into eq 20, and we have

$$\sigma_t^2 = C_2^{\text{NL}}(t) - 2\langle A \rangle C_1^{\text{NL}}(t) - [C_1^{\text{NL}}(t)]^2 + \sigma_{\text{eq}}^2 \quad (22)$$

where $\sigma_{\text{eq}}^2 = \langle A^2 \rangle - \langle A \rangle^2$, and the second-order nonlinear-response cross TCF is given by

$$C_2^{\text{NL}}(t) = \frac{\langle \delta A^2(t) e^{\beta \delta \Delta V(0)} \rangle}{\langle e^{\beta \delta \Delta V} \rangle} \quad (23)$$

Thus, eqs 18 and 22 are the *nonlinear-response* (NLR) prescriptions for the time-dependent average and variance for arbitrary observable, which is exact and no approximations have been applied so far.

Next, we show the linear-response formulas for the time-dependent average and the variance of observable A . For reasons of comprehensiveness, we provide two ways to derive the linear-response expression for IMT. First, we apply the linear approximation for a weak perturbation, i.e., $e^{\beta \delta \Delta V} \approx 1 + \beta \delta \Delta V$,^{71–74} then the two TCFs become

$$\begin{aligned} C_1^L(t) &\approx \frac{\langle \delta A(t)[1 + \beta\delta\Delta V(0)] \rangle}{\langle 1 + \beta\delta\Delta V(0) \rangle} \\ &= \beta\langle \delta A(t)\delta\Delta V(0) \rangle \end{aligned} \quad (24)$$

$$\begin{aligned} C_2^L(t) &\approx \frac{\langle \delta A^2(t)[1 + \beta\delta\Delta V(0)] \rangle}{\langle 1 + \beta\delta\Delta V(0) \rangle} \\ &= \beta\langle \delta A^2(t)\delta\Delta V(0) \rangle \end{aligned} \quad (25)$$

Here, we used the fact that the equilibrium average of a fluctuation vanishes. After truncating after the linear term in β , we arrive at the *linear-response* (LR) expressions:

$$\overline{A(t)} = C_1^L(t) + \langle A \rangle \quad (26)$$

$$\sigma_t^2 = C_2^L(t) - 2\langle A \rangle C_1^L(t) + \sigma_{eq}^2 \quad (27)$$

It should be mentioned that the term $[C_1^{NL}(t)]^2$ is not present in the LR expression of the variance since it is one of the second order terms, and the derivation of quadratic-response (QR) expressions are summarized in [Appendix A](#).

Moreover, a more general assumption of Gaussian distributions in the energy gaps could also lead to the same LR result in [eqs 24 and 25](#),^{61,62} which is summarized below. Assuming $A(t)$ and $\Delta V(t)$ are Gaussian random variables, we can then express the numerator for the $C_1^{NL}(t)$ in [eq 19](#) as

$$\langle \delta A(t)e^{\beta\delta\Delta V(0)} \rangle = \sum_{n=0}^{\infty} \frac{1}{n!} \beta^n \langle \delta A(t)\delta\Delta V(0)^n \rangle \quad (28)$$

Using Wick's theorem,⁷⁵ if $\delta A(t)$ and $\delta\Delta V(t)$ are zero-mean Gaussian random variables, only even-order correlation functions $\langle \delta A(t_0)\delta\Delta V(t_1)\dots\delta\Delta V(t_n) \rangle$ (where $n+1$ is even) survive and can be reduced to the product of all the possible pair correlation functions in terms of $\langle \delta A(t_i)\delta\Delta V(t_j) \rangle$ or $\langle \delta\Delta V(t_i)\delta\Delta V(t_j) \rangle$ ($i \neq j \in \{0, 1, \dots, n\}$). Thus

$$\langle \delta A(t)e^{\beta\delta\Delta V(0)} \rangle \approx \sum_{k=0}^{\infty} \frac{1}{(2k+1)!} \beta^{2k+1} \langle \delta A(t)\delta\Delta V(0)^{2k+1} \rangle \quad (29)$$

where $n = 2k + 1$ and

$$\begin{aligned} &\langle \delta A(t)\delta\Delta V(0)^{2k+1} \rangle \\ &= \frac{(2k+1)!}{k!2^k} \langle \delta A(t)\delta\Delta V(0) \rangle \langle [\delta\Delta V(0)]^2 \rangle^k \end{aligned} \quad (30)$$

Substitute the above result to [eq 29](#)

$$\begin{aligned} \langle \delta A(t)e^{\beta\delta\Delta V(0)} \rangle &\approx \beta\langle \delta A(t)\delta\Delta V(0) \rangle \\ &\quad \sum_{k=0}^{\infty} \frac{1}{k!} \frac{\beta^{2k}}{2^k} \langle [\delta\Delta V(0)]^2 \rangle^k \\ &= \beta\langle \delta A(t)\delta\Delta V(0) \rangle e^{\beta^2 \langle [\delta\Delta V(0)]^2 \rangle / 2} \end{aligned} \quad (31)$$

Since $\delta\Delta V$ is a zero-mean Gaussian random variable, we have

$$\langle e^{\beta\delta\Delta V} \rangle = e^{\beta^2 \langle (\delta\Delta V)^2 \rangle / 2} \quad (32)$$

Finally, taking the ratio of [eqs 31 and 32](#), we arrive at the LR expression that is identical to [eq 24](#)

$$C_1^L(t) = \beta\langle \delta A(t)\delta\Delta V(0) \rangle \quad (33)$$

Similarly, if $\delta A^2(t)$ is a zero-mean Gaussian random variable, one could obtain the $C_2^L(t)$ in [eq 25](#).

The Gaussian version of the linear-response theory broadens its applicability, since it goes beyond the weak perturbation assumption and is expected to be valid as long as the energy gaps are Gaussian, which is supported by the central limit theorem.⁴⁵ On the other hand, LR is also expected to be accurate if the fluctuation of the energy gap is small but non-Gaussian. It is highlighted that the NLR expression ([eqs 18 and 22](#)) relies on neither weak perturbation nor Gaussian statistics, thus is expected to be accurate in all cases.

In IMT, we replace A with $U = U_{DA} = V_D - V_A$ and replace ΔV with $U_{DG} = V_D - V_G$. The current LR and NLR expressions can be directly evaluated with equilibrium molecular dynamics simulation on the donor PES.

3. SIMULATION TECHNIQUES

The all-atom model of the CPC₆₀ triad dissolved in explicit THF was adopted from refs [42](#) and [44](#). For the *bent* and *linear* triad conformations, four electronic-state-dependent force fields were constructed for the ground, $\pi\pi^*$, CT1, and CT2 states. The PESs corresponding to four electronic states of triad differ from one to another by the excitation energies and the atomic partial charges in the triad. The nonelectrostatic interactions are assumed to be the same for different electronic states. The excitation energies, partial charges, and electronic coupling coefficients for this system were computed using time-dependent density functional theory (TDDFT) using the range-separated hybrid Baer-Neuhäuser-Livshits (BNL) functional.^{76–78} The electronic coupling coefficients between the electronically excited states were calculated via the fragment charge difference (FCD) method.⁷⁹ The overall PES in the α th excited state is given by

$$\begin{aligned} V_\alpha(\mathbf{R}) &= V_\alpha^{MD}(\mathbf{R}) + E_\alpha(\mathbf{r}^{\text{Triad}}) - V_{\alpha,T}(\mathbf{r}^{\text{Triad}}) \\ &= V_\alpha^{MD}(\mathbf{R}) + W_\alpha \end{aligned} \quad (34)$$

Here, $E_\alpha(\mathbf{r}^{\text{Triad}})$ is the α th excited state energy with respect to the ground state for the gas-phase triad obtained with electronic structure calculations using the characteristic bent and linear triad geometries, i.e., $\mathbf{r}^{\text{Triad}}$. Since the sum of MD potential energy of the entire system $V_\alpha^{MD}(\mathbf{R})$ and the excitation energy $E_\alpha(\mathbf{r}^{\text{Triad}})$ double counts the triad intramolecular interactions, one needs to subtract this contribution $V_{\alpha,T}(\mathbf{r}^{\text{Triad}})$ calculated using the corresponding force fields with only the triad present, giving rise to the energy correction W_α to the MD potential energy of the α th excited state. [Table 1](#) shows the values of E_α , $V_{\alpha,T}$, and W_α for the $\pi\pi^*$, CT1, and CT2 states in the bent and linear conformations. For details of

Table 1. Energy Correction W_α Defined As the Difference between the Excitation Energy E_α and Triad-Only Force Field Potential Energy $V_{\alpha,T}$ for Each Excited State $\alpha = \pi\pi^*$, CT1, CT2 of the Triad in the Bent and Linear Conformations (eV)

state (α)	conf	E_α	$V_{\alpha,T}$	W_α
$\pi\pi^*$	bent	1.840	1.010	0.830
	linear	2.180	0.598	1.582
CT1	bent	1.771	3.957	-2.186
	linear	2.450	3.630	-1.140
CT2	bent	2.360	3.817	-1.457
	linear	2.539	3.725	-1.186

force field parameters, we refer the reader to refs 41, 43, and 44.

MD simulations were performed for a system containing one triad molecule and 6741 THF molecules in a $100 \text{ \AA} \times 100 \text{ \AA} \times 100 \text{ \AA}$ periodic cubic box, performed using the AMBER 18 package.⁸⁰ Particle mesh Ewald summation was used to calculate the electrostatic interactions.⁸¹ The van der Waals cutoff radius was set to be 9 Å. The SHAKE algorithm⁸² was used to constrain all covalent bonds involving hydrogen atoms. To maintain the linear triad conformation, the end-to-end distance was constrained at 49.6 Å using a steep harmonic potential with a force constant of 100 kcal mol⁻¹Å⁻². No such constraint was used in the case of the flexible bent conformation. The MD time step was chosen as $\delta t = 1.0 \text{ fs}$. The system was equilibrated on the $\pi\pi^*$ state at 300 K using a Langevin thermostat with collision frequency 1.0 ps⁻¹.

In the equilibrium MD simulations for LR and NLR IMT calculations, 200 independent trajectories of length 500 ps were generated under NVE ensemble, whose initial conditions (both positions and velocities) were sampled every 5 ps from an NVT trajectory at 300 K equilibrated on the $\pi\pi^*$ PES, followed by a 50 ps re-equilibration under constant NVE conditions. Configurations were sampled every 5 fs in these 200 NVE trajectories of 500 ps each, which means a total of 2×10^7 configurations were sampled from equilibrium NVE trajectories of total 100 ns in each case of different triad conformations. The potential energies on every electronic-state PES were recalculated along these trajectories. The error bars were obtained by averaging over 5 blocks of data. Note that only 100 trajectories were needed to obtain a converged LR result, but we report both LR and NLR results obtained from the same 200 trajectories for fair comparison.

It is important to note that the trajectory obtained from NVT simulations with a thermostat was not true Hamiltonian dynamics, which may lead to inaccurate TCFs, but fine for sampling. It is suggested to benchmark the TCFs from the NVT trajectory against the TCFs from the NVE trajectory before using NVT simulations for TCF calculations. To test if NVT simulations could offer reasonable predictions for IMT rates, the above-mentioned simulation strategy was also used to generate 400 NVT trajectories of 100 ps each, except for using a thermostat in both sampling and trajectory generating phases. For the current triad system, NVT simulations give rise to the same TCFs as those obtained from NVE simulations.

In the NEMD simulations for obtaining the benchmarking IMT result, a total of 2×10^4 nonequilibrium NVE trajectories was initially sampled from an equilibrated ground state in the NVT ensemble at 300 K and propagated for 4 ps under constant NVE conditions with the configuration recorded every time step, i.e. 1.0 fs. Thus, a total sum of 8×10^7 nonequilibrium configurations were averaged over to obtain the IMT rate coefficient.³²

The nonlinear-response average donor–acceptor energy gap and its variance for IMT rates (eq 12) are given by

$$\bar{U}_t = C_1^{\text{NL}}(t) + \langle U_{DA} \rangle \quad (35)$$

$$\sigma_t^2 = C_2^{\text{NL}}(t) - 2\langle U_{DA} \rangle C_1^{\text{NL}}(t) - [C_1^{\text{NL}}(t)]^2 + \sigma_{\text{eq}}^2 \quad (36)$$

where

$$C_1^{\text{NL}}(t) = \frac{\langle \delta U_{DA}(t) e^{\beta \delta U_{DG}(0)} \rangle}{\langle e^{\beta \delta U_{DG}} \rangle} \quad (37)$$

$$C_2^{\text{NL}}(t) = \frac{\langle \delta U_{DA}^2(t) e^{\beta \delta U_{DG}(0)} \rangle}{\langle e^{\beta \delta U_{DG}} \rangle} \quad (38)$$

and the variance of fluctuating donor–acceptor energy gap in the equilibrated donor state $\sigma_{\text{eq}}^2 = \langle U_{DA}^2 \rangle - \langle U_{DA} \rangle^2$. The linear-response estimations for these parameters are given by

$$\bar{U}_t = C_1^{\text{L}}(t) + \langle U_{DA} \rangle \quad (39)$$

$$\sigma_t^2 = C_2^{\text{L}}(t) - 2\langle U_{DA} \rangle C_1^{\text{L}}(t) + \sigma_{\text{eq}}^2 \quad (40)$$

where

$$C_1^{\text{L}}(t) = \beta \langle \delta U_{DA}(t) \delta U_{DG}(0) \rangle \quad (41)$$

$$C_2^{\text{L}}(t) = \beta \langle \delta U_{DA}^2(t) \delta U_{DG}(0) \rangle \quad (42)$$

Table 2 summarizes the equilibrium averages of the energy gap between different pairs of PESs and its equilibrium variances calculated using the equilibrium MD trajectories generated on the $\pi\pi^*$ state. The magnitude of the energy gap fluctuations between $\pi\pi^*$ and CT2 states are the largest of all three cases, and this can be understood by realizing CT2 has the longest CT across the entire triad making the difference in the potential energy of CT2 relative to the $\pi\pi^*$ state the largest on average and also its fluctuation, since the most solvent molecules are affected by the partial charge differences between two states. For the same reason, both of the $\pi\pi^*$ and the ground states do not have significant CT, and therefore the fluctuation of their energy gap is the smallest.

4. RESULTS AND DISCUSSION

We present the comparison of LR, NLR, and NEMD approaches to compute the time-dependent IMT rate coefficients for two photoinduced CT processes involving $\pi\pi^* \rightarrow \text{CT1}$ (shorthand for eq 4) and $\pi\pi^* \rightarrow \text{CT2}$ (shorthand for eq 5) in two characteristic triad conformations, i.e. flexible bent and linear triads dissolved in explicit THF. From our previous study, the first photoinduced CT process in the bent triad shows a significant nonequilibrium effect in the transient CT rate coefficient, and freezing the intramolecular motions of the triad does not change the LSC NE-FGR or IMT photoinduced CT dynamics as compared with the flexible triad models that we use here, thereby the transient effects in the time-dependent CT rates originate from the non-equilibrium relaxation of the solute–solvent interactions.³² Linear-response theory is known to be widely applicable to the solvation dynamics problems, where nonequilibrium relaxation can be described by an equilibrium time autocorrelation function of the energy gap between the excited state and the

Table 2. Average Energy Gap ($\langle U_{XY} \rangle$, eV), Average Squared Energy Gap ($\langle U_{XY}^2 \rangle$, eV²), and Variance of U_{XY} (σ_{eq}^2 , eV²) between Different Pairs of Potential Energy Surfaces (X–Y) in the Bent and Linear Triad Conformations As Obtained from Equilibrium MD Simulations on the $\pi\pi^*$ State

X–Y	conf	$\langle U_{XY} \rangle$	$\langle U_{XY}^2 \rangle$	σ_{eq}^2
$\pi\pi^*-\text{CT1}$	bent	0.493 ± 0.018	0.271 ± 0.018	0.028 ± 0.002
$\pi\pi^*-\text{CT1}$	linear	-0.166 ± 0.017	0.063 ± 0.005	0.036 ± 0.002
$\pi\pi^*-\text{CT2}$	bent	-0.421 ± 0.053	0.256 ± 0.046	0.075 ± 0.004
$\pi\pi^*-\text{CT2}$	linear	-0.416 ± 0.019	0.262 ± 0.161	0.089 ± 0.004
$\pi\pi^*-\text{G}$	bent	1.598 ± 0.011	2.560 ± 0.035	0.005 ± 0.001
$\pi\pi^*-\text{G}$	linear	1.986 ± 0.019	3.958 ± 0.073	0.014 ± 0.003

ground state, whereas, in the IMT case, the expressions involve cross correlation functions of the energy gaps between different pairs of PESs. Moreover, the nonequilibrium variance in the energy gap is expressed in terms of the cross correlation functions of the fluctuations of the donor–acceptor energy gap squared and the donor–ground energy gap. These features of the newly developed formulas for calculating IMT using only equilibrium MD simulations are desirable and worth testing.

First of all, we discuss the results of the bent triad conformation. Figure 2 is one of our main results, which shows the comparison of the IMT rate coefficients calculated from the LR and NLR via equilibrium MD simulations as well as IMT rate coefficients from the direct NEMD simulations for the bent triad conformation. Here, the IMT rate coefficients from NEMD were reproduced from ref 32. In general, both LR and NLR give reasonable predictions to the transient CT rate coefficients in $\pi\pi^* \rightarrow \text{CT1}$ and $\pi\pi^* \rightarrow \text{CT2}$ processes, compared with those obtained from NEMD. The trend during the first 4 ps after the photoexcitation exhibits that \bar{U}_t increases with time from about 0.17 eV to 0.5 eV for the $\pi\pi^* \rightarrow \text{CT1}$ transition and from about -0.55 eV to -0.40 eV for the $\pi\pi^* \rightarrow \text{CT2}$ transition, respectively, as well as that σ_t^2 simply fluctuates around its mean values of 0.028 and 0.075 eV² for the $\pi\pi^* \rightarrow \text{CT1}$ and the $\pi\pi^* \rightarrow \text{CT2}$ transitions, respectively. Consequently, the IMT rate coefficient decreases with time for the $\pi\pi^* \rightarrow \text{CT1}$ process since the \bar{U}_t is positive and increasing in magnitude, whereas for the $\pi\pi^* \rightarrow \text{CT2}$ process, the IMT rate coefficient increases slightly with time, noting that for this case the \bar{U}_t is negative and decreasing in magnitude (see eq 12). The fact that the instantaneous CT rate coefficient shows

strong time-dependence indicates significant nonequilibrium effects due to the initial preparation of the nuclear DOF in the bent triad case.

In a sense, NLR being able to get the right IMT result is not surprising, since it is based on the exact expressions of the nonequilibrium average donor–acceptor energy gap \bar{U}_t and its variance σ_t^2 . On the other hand, NLR is surprisingly remarkable in the aspect of being able to converge the TCFs with only a doubled amount of trajectories that are required for LR, considering that the exponential of the fluctuation in the donor–ground energy gap, i.e. $\exp(\beta\delta\Delta V)$ in $C_{1/2}^{\text{NL}}(t)$, might weigh more toward the positive fluctuations than the negative ones.

However, LR slightly overestimates the CT rate coefficients in the $\pi\pi^* \rightarrow \text{CT1}$ process, which is directly caused by the underestimated \bar{U}_t . The fact that \bar{U}_t via LR slightly deviates from the exact NLR suggests mild breakdown of the linear-response theory, which can be traced back to the slightly non-Gaussian and noticeable fluctuating donor–ground energy gap ΔV , because if ΔV is strictly Gaussian, LR would be exactly the same as NLR, and also in the $\pi\pi^* \rightarrow \text{CT1}$ process $\beta\delta\Delta V$ could have extreme values larger than 1 despite its mean value is zero. To justify the perturbative treatment, we show in Figure 3 that the linear term in the power expansion in $\langle e^{\beta\delta\Delta V(0)}\delta A(t) \rangle$ and $\langle e^{\beta\delta\Delta V(0)}\delta A^2(t) \rangle$ is the dominant and any term beyond the second order in the power expansions of $\exp(\beta\delta\Delta V)$ in $C_{1/2}^{\text{NL}}(t)$, namely $(\beta^n/n!)\langle\delta\Delta V^n(0)\delta A(t)\rangle$ and $(\beta^n/n!)\langle\delta\Delta V^n(0)\delta A^2(t)\rangle$ ($n > 2$), is relatively much smaller than the linear term. However, the deviation from the Gaussian

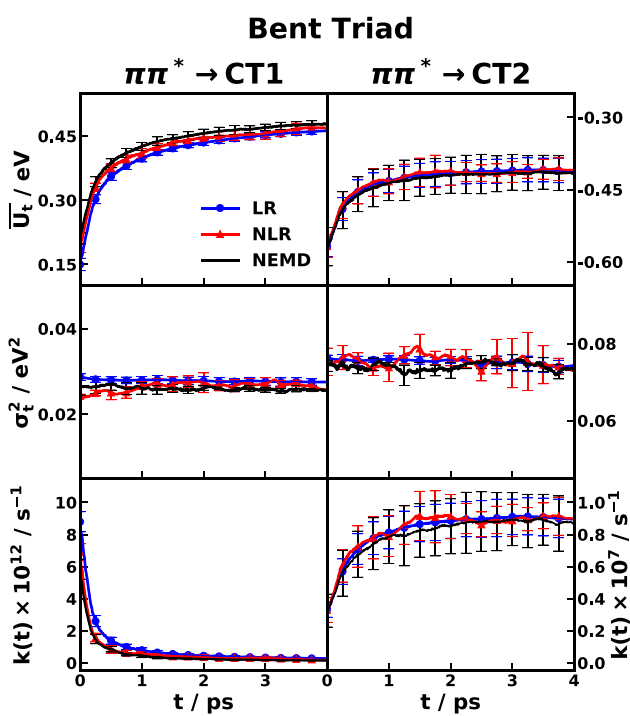


Figure 2. Comparison of time-dependent nonequilibrium average of donor–acceptor energy gap \bar{U}_t (top), its variance σ_t^2 (middle), and IMT rate coefficient $k(t)$ (bottom) for the transitions $\pi\pi^* \rightarrow \text{CT1}$ (left) and $\pi\pi^* \rightarrow \text{CT2}$ (right) in the bent triad conformation obtained with the linear-response (LR), nonlinear-response (NLR), and nonequilibrium MD (NEMD) approaches.

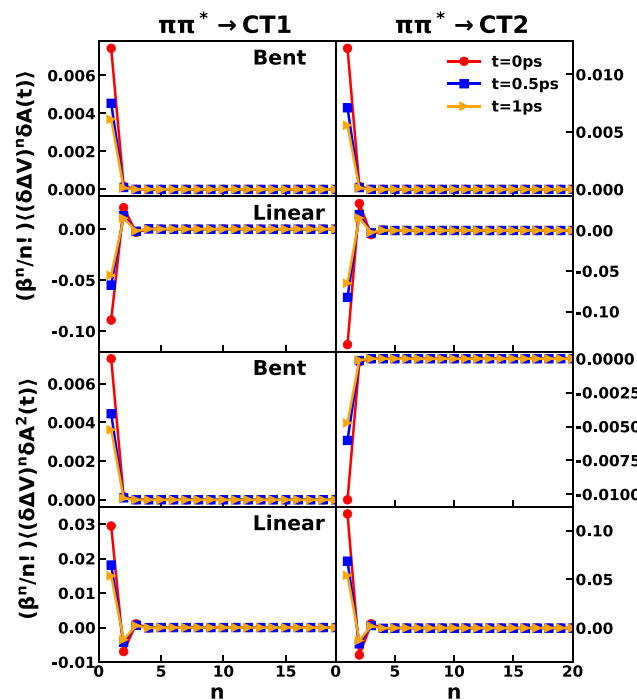


Figure 3. Comparison of contributions to $C_1^{\text{NL}}(t)$ (upper panels) and $C_2^{\text{NL}}(t)$ (lower panels), i.e. $(\beta^n/n!)\langle\delta\Delta V^n(0)\delta A(t)\rangle$ and $(\beta^n/n!)\langle\delta\Delta V^n(0)\delta A^2(t)\rangle$ as a function of the expansion order n , for transitions $\pi\pi^* \rightarrow \text{CT1}$ (left) and $\pi\pi^* \rightarrow \text{CT2}$ (right) in the bent and linear triad conformations. Here, for the IMT, the fluctuations of energy gaps are $\delta\Delta V = \delta U_{DG}$ and $\delta A = \delta U_{DA}$.

statistics and the weak perturbation assumptions is very mild, thus the LR can still capture the predominant response.

The underestimation in \bar{U}_t via LR can be visualized in Figure 4, which depicts the drift of the energy gap distribution along the nonequilibrium relaxation time. It is evident that the analytical energy gap distributions parametrized by \bar{U}_t and σ_t^2 obtained from LR (dashed profile) is slightly red-shifted from the NEMD distribution (histogram and solid profile), whereas the NLR energy gap distributions agree well with the NEMD distributions, except for a bit narrower in width at early time. More importantly, Figure 4 validates the underlying assumption of IMT that the donor–acceptor energy gap ($A = U = U_{DA}$) has a time-dependent Gaussian distribution, and shows that our LR and NLR treatments could capture the correct trend of energy gap distribution change—increasing the mean while maintaining the width.

In fact, Figure 4 shows clearly the difference between the nonequilibrium average of the energy gap fluctuations about its *nonequilibrium average* ($A(t) - \bar{A}(t)$) defined in eq 20 and the nonequilibrium average of the energy gap fluctuations about its *equilibrium average* ($\delta A(t) = A(t) - \langle A \rangle$) defined as below

$$\begin{aligned} [\delta A(t)]^2 &= [A(t) - \langle A \rangle]^2 \\ &= \overline{A^2(t)} - 2\langle A \rangle \overline{A(t)} + \langle A \rangle^2 \\ &= C_2^{NL}(t) - 2\langle A \rangle C_1^{NL}(t) + \sigma_{eq}^2 \end{aligned} \quad (43)$$

The time-dependent variance used in IMT is about the nonequilibrium average \bar{U}_t , which changes from 0.15 to 0.45 eV in $\pi\pi^* \rightarrow CT1$ in bent triad, while the equilibrium average

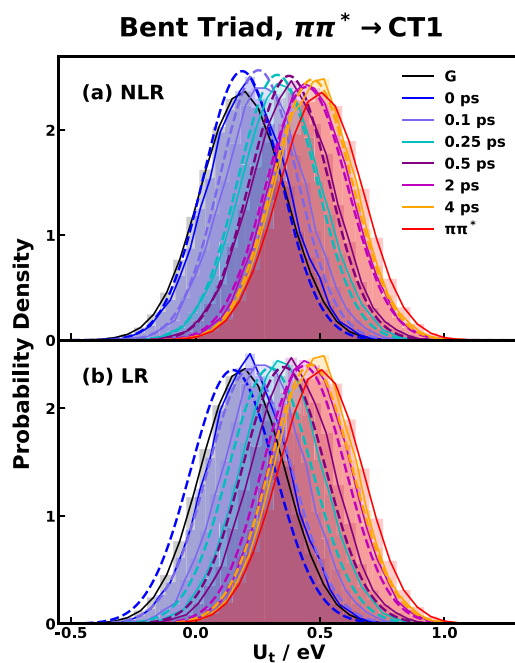


Figure 4. Probability distributions of the donor–acceptor energy gap (\bar{U}_t) for transition $\pi\pi^* \rightarrow CT1$ in the bent triad conformation at different times following the vertical excitation from the ground (G) state onto the $\pi\pi^*$ state. The histograms and the solid lines are distributions obtained from 20 000 nonequilibrium MD trajectories, and dashed lines correspond to the analytical Gaussian distribution calculated using eq 11 where the time-dependent mean \bar{U}_t and variance σ_t^2 were extracted from the NLR (a) or LR (b) predictions.

$\langle U \rangle$ is a constant of about 0.49 eV. The difference between σ_t^2 in eq 20 and $[\delta A(t)]^2$ in eq 43 is that σ_t^2 has an extra $[C_1^{NL}(t)]^2$ term, which is coming from the difference in the average definition.

If we naïvely take the linear approximation of the TCFs in eq 43, we could obtain the same expression as the LR for IMT in eq 27. Does that mean the LR is measuring the fluctuations about the equilibrium averages? The answer is no. Actually, the LR still measures the fluctuations about the nonequilibrium average and it should just contain the linear contribution to the full-order NLR expression. Although we define the LR TCFs using the fluctuations about the equilibrium average $\langle A \rangle$, it is only a convenient choice such that we can use $\langle \delta A(t) \rangle = 0$. Admittedly, one can define the fluctuations with respect to any constant, such as $\tilde{\delta}A(t) = A(t) - \overline{A(0)}$, the nonequilibrium average of A at time t in LR would be

$$\overline{A(t)} = \tilde{C}_1^L(t) + \overline{A(0)} = \beta \langle \tilde{\delta}A(0) \delta \Delta V(0) \rangle + \langle A \rangle \quad (44)$$

where

$$\begin{aligned} \tilde{C}_1^L(t) &= \beta \langle \tilde{\delta}A(0) \delta \Delta V(0) \rangle + \langle \tilde{\delta}A(t) \rangle \\ &= \beta \langle \tilde{\delta}A(0) \delta \Delta V(0) \rangle + \langle A \rangle - \overline{A(0)} \end{aligned} \quad (45)$$

Since $\langle \tilde{\delta}A(0) \delta \Delta V(0) \rangle = \langle \delta A(0) \Delta \delta V(0) \rangle \langle A(0) \delta \Delta V(0) \rangle$ as long as $\langle \delta \Delta V \rangle = 0$, eq 44 is equivalent to LR expression in eq 26, meaning that the time dependence will be captured by TCF with fluctuations in $A(t)$ about an arbitrary reference constant. So we conclude that eq 43 is not the correct definition for time-dependent variance of energy gap in IMT, even though it seems to give the LR expressions in eq 27 at first glance. Therefore, the $-[C_1^{NL}(t)]^2$ term in NLR (eq 22) is due to the fact that we are measuring the fluctuations about the nonequilibrium average that changes during the relaxation.

Next, we show why the $-[C_1^L(t)]^2$ term should be neglected in the LR expression of the time-dependent variance $\sigma_t^2 = \overline{A^2(t)} - [\overline{A(t)}]^2$ by comparing different TCFs in LR, NLR, and the quadratic response (QR) expressions, where the derivation of QR is included in Appendix A. The LR, QR, and NLR expressions for the nonequilibrium average of the energy gap (eqs 26, A.1, and 18) are summarized as below

$$\begin{aligned} \overline{A(t)}(\text{LR}) &= C_1^L(t) + \langle A \rangle \\ \overline{A(t)}(\text{QR}) &= C_1^L(t) + C_1^Q(t) + \langle A \rangle \\ \overline{A(t)}(\text{NLR}) &= C_1^{NL}(t) + \langle A \rangle \end{aligned} \quad (46)$$

and the corresponding variance (eqs 27, A.4, and 22) are

$$\begin{aligned} \sigma_t^2(\text{LR}) &= C_2^L(t) - 2\langle A \rangle C_1^L(t) + \sigma_{eq}^2 \\ \sigma_t^2(\text{QR}) &= C_2^L(t) - 2\langle A \rangle C_1^L(t) + \sigma_{eq}^2 \\ &\quad + C_2^Q(t) - [C_1^L(t)]^2 - 2\langle A \rangle C_1^Q(t) \\ \sigma_t^2(\text{NLR}) &= C_2^{NL}(t) - 2\langle A \rangle C_1^{NL}(t) - [C_1^{NL}(t)]^2 + \sigma_{eq}^2 \end{aligned} \quad (47)$$

Figure 5 shows the $C_1(t)$ and $C_2(t)$ in LR, QR, and NLR for transitions $\pi\pi^* \rightarrow CT1$ and $\pi\pi^* \rightarrow CT2$ in the bent triad. Here, the $C_1^{L/NL}(t)$ reflects the trend of increasing \bar{U}_t and $C_1^Q(t)$ is almost zero in both transitions, which are expected and agree with the NEMD IMT as shown in the top left panel of Figure 6. The top right panel of Figure 6 shows the very small second-

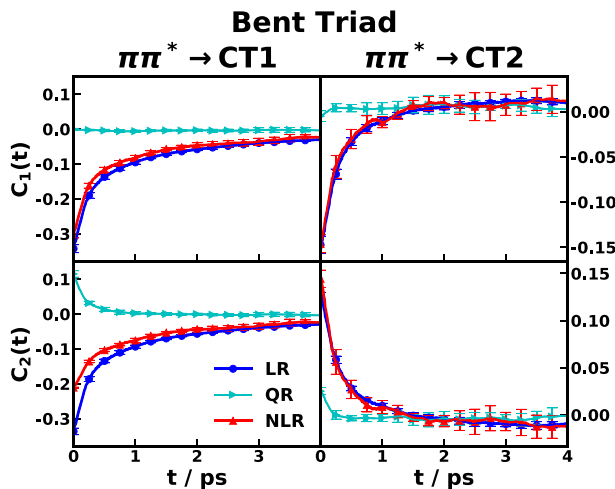


Figure 5. Time correlation functions $C_1(t)$ and $C_2(t)$ in linear-response (LR), quadratic response (QR), and nonlinear-response (NLR) expressions of IMT for transitions $\pi\pi^* \rightarrow \text{CT1}$ (left) and $\pi\pi^* \rightarrow \text{CT2}$ (right) in the bent triad conformation.

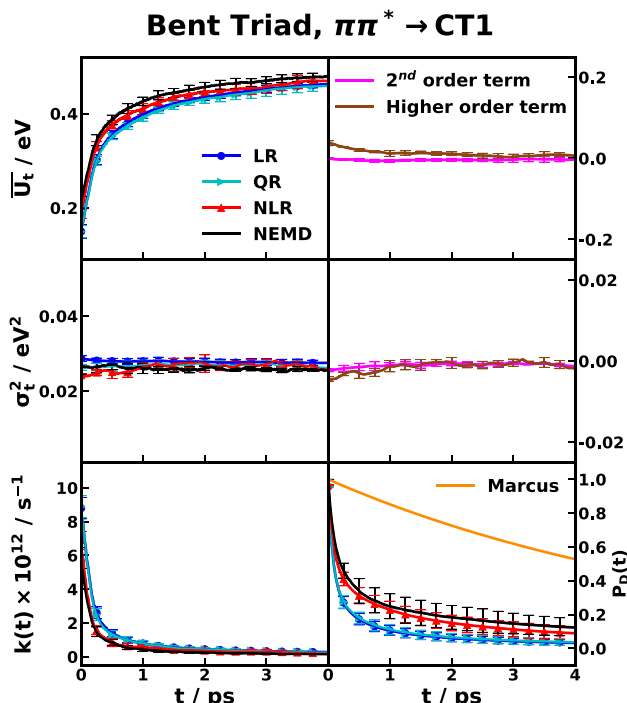


Figure 6. Comparison of \bar{U}_t (top), σ_t^2 (middle), IMT rate coefficient $k(t)$ (bottom left), and donor-state population $P_D(t)$ (bottom right) for the $\pi\pi^* \rightarrow \text{CT1}$ transition in the bent triad conformation computed using linear-response (LR), quadratic response (QR), and nonlinear-response (NLR) expressions of IMT and those from nonequilibrium MD (NEMD) simulations. The second-order term (top right) and the higher order terms (middle right) are obtained by subtracting LR contributions from QR and NLR expressions, respectively. The orange line is the exponential donor-state population decay predicted using a Marcus rate constant as obtained from equilibrium MD simulations on the $\pi\pi^*$ state, which lacks the treatment for nonequilibrium initial conditions.

order term $C_1^Q(t)$ and the nonvanishing higher-order terms $C_1^{\text{NL}}(t) - C_1^L(t)$ for \bar{U}_t , which means that the discrepancy of LR

is not primarily from neglecting the second-order term but from neglecting all the tiny but nonvanishing higher-order terms in the expansion of $\exp(\beta\delta\Delta V)$ in $C_1^{\text{NL}}(t)$ (see Figure 3).

Moreover, the time-independent behavior of σ_t^2 predicted from LR, QR, and NLR displayed in the middle panels in Figure 6 can be broken down to terms of TCFs in Figure 5. In the second-order correction to LR, i.e. $C_2^Q(t) - [C_1^L(t)]^2 - 2\langle A \rangle C_1^Q(t)$ terms in QR, $C_2^Q(t)$ and $-[C_1^L(t)]^2$ cancel with each other and the last term vanishes, so the second order correction to the σ_t^2 eventually vanishes. In other words, the $-[C_1^L(t)]^2$ term is one of the second-order terms and the sum of second-order terms vanishes, so LR should not include the $-[C_1^L(t)]^2$ term. The higher-order correction to LR σ_t^2 also vanishes, i.e. the difference between NLR and LR $C_2^{\text{NL}}(t) - [C_1^{\text{NL}}(t)]^2 - C_2^L(t) - 2\langle A \rangle [C_1^{\text{NL}}(t) - C_1^L(t)] \approx 0$, which suggests the importance of including $-[C_1^{\text{NL}}(t)]^2$ in the NLR expression for σ_t^2 . As shown in bottom panels in Figure 6, the time-dependent IMT rate and the donor-state population as obtained with LR, QR, and NLR could faithfully reproduce the general trend of the exact NEMD result that manifests much faster CT dynamics than that predicted by the Marcus rate constant, while the identical LR and QR overestimate the transient CT rate coefficient because of neglecting higher orders of $\exp(\beta\delta\Delta V)$ in the $\pi\pi^* \rightarrow \text{CT1}$ transition in the bent triad.

In addition, we comment on the trend of TCFs $C_{1/2}^{\text{L/NL}}(t)$ shown in Figure 5. $C_1^{\text{L/NL}}(t)$ is increasing from a negative value to zero in both $\pi\pi^* \rightarrow \text{CT1}$ and $\pi\pi^* \rightarrow \text{CT2}$ transitions in the bent triad, which can be rationalized by referring to Figure 1c: following the vertical photoexcitation both $V_{\pi\pi^*} - V_{\text{CT1}}$ and $V_{\pi\pi^*} - V_{\text{CT2}}$ increase to their equilibrium averages, thus $\delta U_{DA}(t)$ is a negative number approaching zero at long time, leading to an anticorrelation between $\delta U_{DG}(0)$ and $\delta U_{DA}(t)$. However, the trend of $C_2^{\text{L/NL}}(t)$ is opposite in the cases of $\pi\pi^* \rightarrow \text{CT1}$ and $\pi\pi^* \rightarrow \text{CT2}$, which can be traced back to the fact that for the bent triad the square of the positive energy gap $V_{\pi\pi^*} - V_{\text{CT1}}$ is increasing but the square of the negative $V_{\pi\pi^*} - V_{\text{CT2}}$ is decreasing along the relaxation, leading to an anticorrelation between $\delta U_{DG}(0)$ and $\delta U_{DA}^2(t)$ in the case of $\pi\pi^* \rightarrow \text{CT1}$ whereas a correlation exists between $\delta U_{DG}(0)$ and $\delta U_{DA}^2(t)$ in the $\pi\pi^* \rightarrow \text{CT2}$ case, respectively.

The corresponding trends of the instantaneous Marcus parameters in the bent triad conformation, namely the time-dependent reorganization energy $E_r(t)$, reaction free energy $\Delta E(t)$, and activation energy $E_a(t)$ are shown in Figure 7. These parameters are calculated from \bar{U}_t and σ_t^2 via eq 13 and

$$E_a(t) = k_B T (\bar{U}_t)^2 / (2\sigma_t^2) \quad (48)$$

For both transitions $\pi\pi^* \rightarrow \text{CT1}$ and $\pi\pi^* \rightarrow \text{CT2}$, E_r is stationary, which reflects the stationary σ_t^2 , while ΔE is decreasing due to the drifting of \bar{U}_t . The instantaneous activation energy E_a is shown to increase from 0.01 to 0.10 eV for the $\pi\pi^* \rightarrow \text{CT1}$ transition and slightly decrease from 0.06 to 0.04 eV for the $\pi\pi^* \rightarrow \text{CT2}$ transition. From eq 48, the activation energy E_a is proportional to the square of \bar{U}_t and thus increases in the $\pi\pi^* \rightarrow \text{CT1}$ transition leading to a decrease in IMT rate coefficient, while E_a decreases in the $\pi\pi^* \rightarrow \text{CT2}$ transition leading to an increase in IMT rate coefficient. Overall, LR and NLR predict the trends of the three parameters from NEMD; however, NLR starts to slightly underestimate E_a from 1 ps and on, and LR underestimates E_a at all times in the $\pi\pi^* \rightarrow \text{CT1}$ transition.

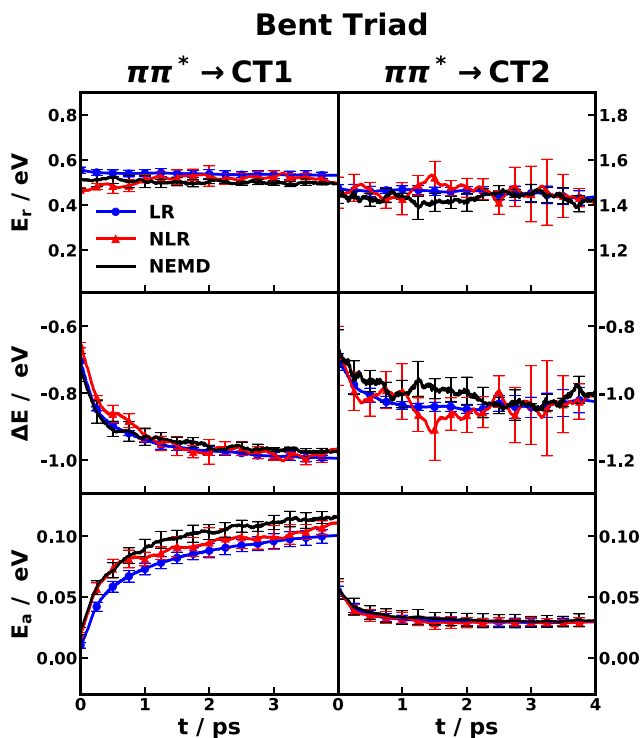


Figure 7. Instantaneous reorganization energy E_r (top), reaction free energy ΔE (middle), and activation energy E_a (bottom) for transitions $\pi\pi^* \rightarrow \text{CT1}$ (left) and $\pi\pi^* \rightarrow \text{CT2}$ (right) in the bent triad conformation.

Second, we discuss the results of the linear triad conformation. As shown in Figure 8, there is no significant nonequilibrium effect in \bar{U}_t , σ_t^2 , and thus $k(t)$ for both $\pi\pi^* \rightarrow \text{CT1}$ and $\pi\pi^* \rightarrow \text{CT2}$ transitions in the linear triad conformation, which can be traced back to the fact that the vertical excitation from the equilibrated ground state is very close to the minimum of the donor-state PES. Both LR and NLR produce the exact stationary NEMD trends in \bar{U}_t and σ_t^2 . Thus, the linear triad conformation serves as a control group, in which we expect that the photoinduced CT dynamics from IMT should agree with the conventional Marcus rate constant. Figure 9 shows the donor-state population decay in the bent and the linear triad conformations, and the IMT result of the linear triad agrees well with the exponential decay from the Marcus rate constant during the 4 ps relaxation, indicating a negligible nonequilibrium effect due to the initial preparation (thus a rate constant would suffice); whereas the bent triad shows very different behavior between IMT (LR, NLR, NEMD) and the Marcus rate constant in the $\pi\pi^* \rightarrow \text{CT1}$ transition as discussed before, yet similar behavior in the $\pi\pi^* \rightarrow \text{CT2}$ transition.

It is noted that, although the $k(t)$ obtained with NLR agrees with the original NEMD in all the cases studied here, the \bar{U}_t of NLR shows a slight deviation from the NEMD approach in the $\pi\pi^* \rightarrow \text{CT1}$ in the bent triad case, which can be attributed to the sensitivity to the initial structural sampling, which is from the ground state for NEMD approach, whereas from the $\pi\pi^*$ (donor) state for NLR approach. This sensitivity is the consequence of the relatively large nonequilibrium relaxation in the bent triad as well as small reorganization energy or fluctuations in the energy gaps (thus small relative error bars), which is due to the shorter range charge redistribution in $\pi\pi^*$

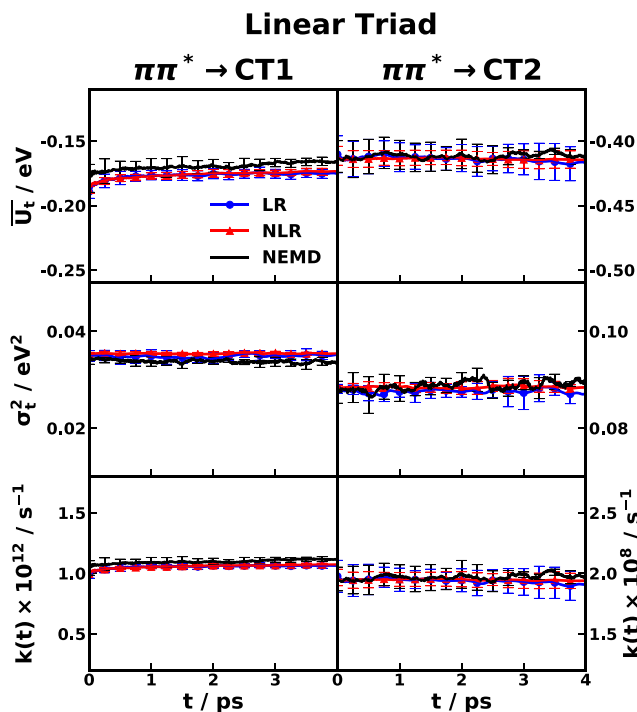


Figure 8. Comparison of time-dependent nonequilibrium average of donor–acceptor energy gap \bar{U}_t (top), its variance σ_t^2 (middle), and IMT rate coefficient $k(t)$ (bottom) for the transitions $\pi\pi^* \rightarrow \text{CT1}$ (left) and $\pi\pi^* \rightarrow \text{CT2}$ (right) in the linear triad conformation obtained with linear-response (LR), nonlinear-response (NLR), and nonequilibrium MD (NEMD) approaches.

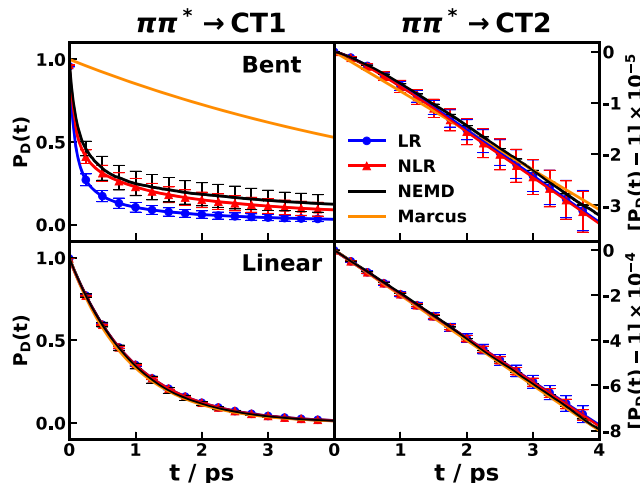


Figure 9. Donor-state population decay $P_D(t)$ for transitions $\pi\pi^* \rightarrow \text{CT1}$ (left) and $\pi\pi^* \rightarrow \text{CT2}$ (right) in the bent triad (top) and linear triad (bottom) conformations. The orange line is predicted by the Marcus rate constant.

$\rightarrow \text{CT1}$ that involves less solvents than in the longer range charge redistribution in $\pi\pi^* \rightarrow \text{CT2}$ that involves more solvents.

For completeness, we show the $C_1(t)$ and $C_2(t)$ in LR, QR, and NLR for transitions $\pi\pi^* \rightarrow \text{CT1}$ and $\pi\pi^* \rightarrow \text{CT2}$ in the linear triad conformation in Figure 10, where the LR and NLR are converged with small error bars but the QR is noisier. Considering the noisy TCFs in the linear triad case and the observation in the bent triad that QR does not improve LR

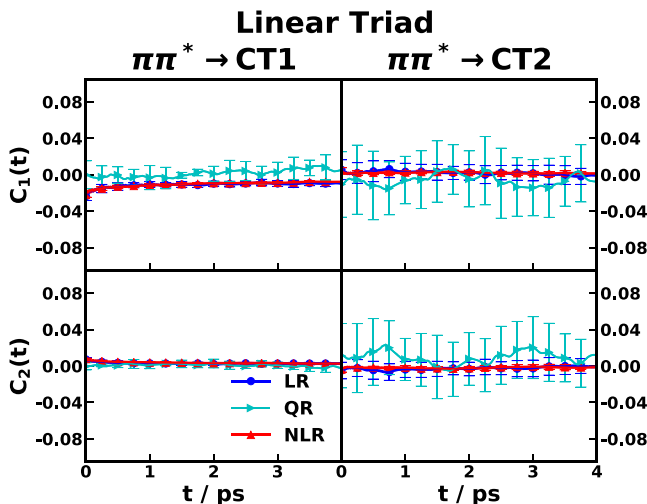


Figure 10. Correlation functions $C_1(t)$ and $C_2(t)$ in linear-response (LR), quadratic response (QR), and nonlinear-response (NLR) theories for transitions $\pi\pi^* \rightarrow CT1$ (left) and $\pi\pi^* \rightarrow CT2$ (right) in the linear triad conformation.

result at all, we generally do not recommend QR for IMT calculation. Figure 11 shows the trends of the instantaneous Marcus parameters $E_r(t)$, $\Delta E(t)$, and $E_a(t)$ in the linear triad conformation, which are mostly constants within error bars as obtained from LR, NLR, and NEMD.

Lastly, we comment on the computational acceleration of using the LR and NLR formalism for computing IMT parameters via equilibrium MD simulations, which allow us to take advantage of the time translational symmetry as compared with the NEMD simulations. To obtain the IMT

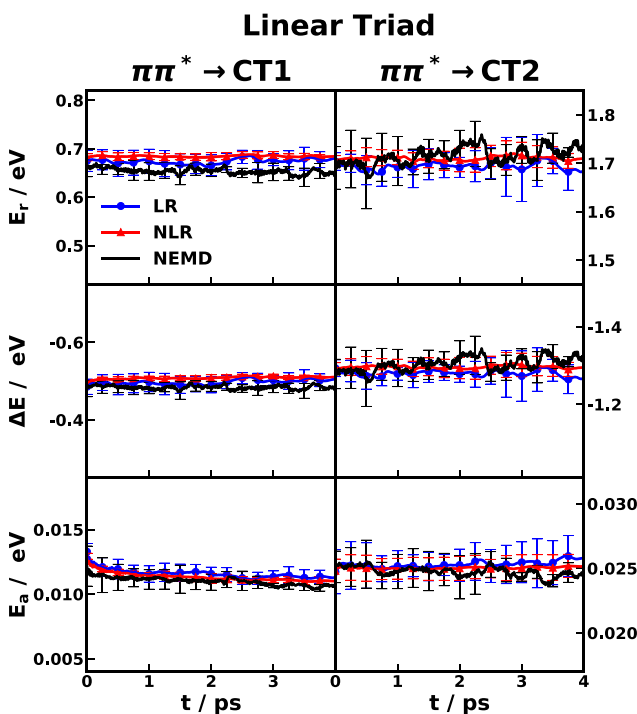


Figure 11. Instantaneous reorganization energy E_r (top), reaction free energy ΔE (middle), and activation energy E_a (bottom) for transitions $\pi\pi^* \rightarrow CT1$ (left) and $\pi\pi^* \rightarrow CT2$ (right) in the linear triad conformation.

result for a single triad conformation, we generated a total sampling time of 80 and 100 ns in our nonequilibrium and equilibrium MD simulations, respectively. The corresponding computational expenditures for the nonequilibrium and equilibrium MD simulations were 196 000³² and 78 400 CPU core-hours, respectively, both implemented using Intel Xeon Gold 6132 @ 2.60 GHz (28 cores) CPU. The advantage of LR is that only half of MD trajectories are required to obtain convergence as compared with NLR, although we reported both results using the same 200 trajectories for fair comparison. Utilizing the time translational symmetry, our LR and NLR methods could reduce the computational cost for obtaining the IMT rate coefficients by 80% and 60%, respectively. Also, LR and NLR can be computed at the same time with negligible overhead. To further accelerate the computation, we also tested a hybrid GPU–CPU approach for equilibrium MD simulations. In this hybrid approach, the trajectory generation were performed using GPU platform and the energy recalculation were performed using improved algorithm on CPU platform. The hybrid approach enabled us to obtain the same result with further reduction in computational expenditure down to 200 GPU core-hours and 33 600 CPU core-hours, which was reduced by 83% for NLR and 92% for LR compared with NEMD. It is also noted that parallel calculations could be straightforwardly applied to both equilibrium MD simulations and NEMD simulations, which start out with independent initial conditions on different high-performance-computing nodes.

It is also worth mentioning that the window length of the time correlation functions $C_{1/2}^{L/NL}(t)$ could be adjusted as necessary according to the time scale of the process being investigated. This means that using the LR and NLR methods for IMT calculation, observation for a longer correlation time (e.g., 100 ps) is straightforward and no additional computational cost will incur. This is a highly desirable trait that allows us to investigate slow relaxation processes in complex systems involving large molecule or biological entity.

5. CONCLUDING REMARKS

In this paper, we have derived the linear-response (LR) and nonlinear-response (NLR) formalisms of the instantaneous Marcus theory (IMT) for capturing transient photoinduced charge transfer (CT) dynamics following the photoexcitation that creates a nonequilibrium nuclear initial condition. The derived LR IMT and NLR IMT methods were applied to predict the nonequilibrium photoinduced CT dynamics in the carotenoid–porphyrin–C₆₀ (CPC₆₀) molecular triad dissolved in explicit tetrahydrofuran (THF) solvent, a photovoltaic energy harvesting system. We benchmarked the time-dependent CT rate coefficients obtained using LR IMT and NLR IMT methods with the full-blown IMT rate coefficient via nonequilibrium molecular dynamics (NEMD) for $\pi\pi^* \rightarrow CT1$ and $\pi\pi^* \rightarrow CT2$ transitions in the bent and linear triad conformations with the nuclear initial conditions sampled from equilibrium ground state. Our result shows that the NLR IMT method yields an excellent prediction for the nonequilibrium IMT CT rate coefficients in all cases investigated here, whereas the LR IMT method could predict the correct trends of the CT rate coefficient but overestimate the transient IMT CT rate in the case where we see the most significant nonequilibrium effect, i.e. $\pi\pi^* \rightarrow CT1$ transition in the bent triad conformation.

To further understand the origin of the mild breakdown of linear-response theory in the IMT rate calculations, we inspected different cross time correlation functions between the fluctuations of the donor–acceptor energy gap and the donor-ground energy gap in LR, QR, and NLR calculations. The evidence reveals that the origin of the mild breakdown can be attributed to the higher-order contributions of \bar{U}_t that are neglected in the LR formalism. In principle, the linear-response theory is expected to be valid if the fluctuations are small or Gaussian;^{45,59,61,62} in our case, the energy gaps seem to have sizable fluctuations and do not strictly follow Gaussian statistics, but the deviation from the assumptions is very small, thus LR still could generate the predominant predictions to the IMT rate. A comprehensive investigation on the mild breakdown of LR for IMT is underway and will be reported in future work.

We conclude by recommending the NLR method of calculating IMT rate coefficients in the photoinduced CT processes that undergo a nonequilibrium relaxation over the less accurate LR method, because the NLR expressions are exact (does not rely on weak perturbation or Gaussian statistics assumptions) and shown agreement with the IMT rates obtained with the NEMD simulations. The advantage of using the NLR or LR approaches is being able to use the time translational symmetry in the equilibrium MD simulations, which could enhance the TCF averaging significantly compared to the NEMD simulations where such symmetry lacks due to the nonequilibrium nature of the dynamics. The benchmark shows that, by using the LR IMT and NLR IMT methods, the computational cost could be reduced by 80% and 60% on the CPU platform and by 92% and 83% on the hybrid CPU–GPU platform, respectively. It is also noted that adding the NLR IMT to LR IMT calculation does not incur extra cost and also both methods could be easily adapted to a much longer correlation time window length with no extra cost. Thus, the readily applicable NLR IMT and LR IMT formalism opens the door to practical simulations of nonequilibrium photoinduced charge transfer dynamics in various complex systems, such as organic photovoltaic molecules in solutions or thin films,^{7–14} luminescent materials,^{83–85} photosynthetic complexes,^{1,4,5} and proteins.^{86,87}

■ APPENDIX A QUADRATIC RESPONSE THEORY FOR IMT

We present the derivation of the quadratic response (QR) expression for IMT. Starting from the full-term nonlinear-response formulas for the time-dependent average as in eq 18, and expanding the exponential to the second order, i.e. $e^{\beta\delta\Delta V} \approx 1 + \beta\delta\Delta V + \frac{1}{2}\beta^2(\delta\Delta V)^2$, we have

$$\begin{aligned} \overline{A(t)} &\approx \frac{\langle \delta A(t) [1 + \beta\delta\Delta V(0) + \frac{1}{2}\beta^2(\delta\Delta V(0))^2] \rangle}{\langle 1 + \beta\delta\Delta V + \frac{1}{2}\beta^2(\delta\Delta V)^2 \rangle} \\ &+ \langle A \rangle \\ &= \beta\langle \delta A(t)\delta\Delta V(0) \rangle + \frac{1}{2}\beta^2\langle \delta A(t)(\delta\Delta V(0))^2 \rangle \\ &+ \langle A \rangle + O((\beta\delta\Delta V)^3) \\ &= C_1^L(t) + C_1^Q(t) + \langle A \rangle \end{aligned} \quad (\text{A.1})$$

where $C_1^L(t)$ is defined in eq 24 and

$$C_1^Q(t) = \frac{1}{2}\beta^2\langle \delta A(t)(\delta\Delta V(0))^2 \rangle \quad (\text{A.2})$$

Apply the second-order approximation to the $\overline{A^2(t)}$ in eq 21, we have

$$\begin{aligned} \overline{A^2(t)} &\approx \frac{\langle \delta A^2(t) [1 + \beta\delta\Delta V(0) + \frac{1}{2}\beta^2(\delta\Delta V(0))^2] \rangle}{\langle 1 + \beta\delta\Delta V + \frac{1}{2}\beta^2(\delta\Delta V)^2 \rangle} \\ &+ \langle A^2 \rangle \\ &= \beta\langle \delta A^2(t)\delta\Delta V(0) \rangle + \frac{1}{2}\beta^2\langle \delta A^2(t)(\delta\Delta V(0))^2 \rangle \\ &+ \langle A^2 \rangle + O((\beta\delta\Delta V)^3) \end{aligned} \quad (\text{A.3})$$

The quadratic response expression for the time-dependent variance is thus given by

$$\begin{aligned} \sigma_t^2 &= \overline{A^2(t)} - [\overline{A(t)}]^2 \\ &\approx \beta\langle \delta A^2(t)\delta\Delta V(0) \rangle + \frac{1}{2}\beta^2\langle \delta A^2(t)(\delta\Delta V(0))^2 \rangle + \langle A^2 \rangle \\ &- \left[\beta\langle \delta A(t)\delta\Delta V(0) \rangle + \frac{1}{2}\beta^2\langle \delta A(t)(\delta\Delta V(0))^2 \rangle + \langle A \rangle \right]^2 \\ &= \sigma_{\text{eq}}^2 + \beta[\langle \delta A^2(t)\delta\Delta V(0) \rangle - 2\langle A \rangle\langle \delta A(t)\delta\Delta V(0) \rangle] \\ &+ \beta^2\left[\frac{1}{2}\langle \delta A^2(t)(\delta\Delta V(0))^2 \rangle - \langle \delta A(t)\delta\Delta V(0) \rangle^2 \right. \\ &\quad \left. - \langle A \rangle\langle \delta A(t)(\delta\Delta V(0))^2 \rangle \right] + O((\beta\delta\Delta V)^3) \\ &= \sigma_{\text{eq}}^2 + C_2^L(t) - 2\langle A \rangle C_1^L(t) + C_2^Q(t) - [C_1^L(t)]^2 - 2\langle A \rangle C_1^Q(t) \end{aligned} \quad (\text{A.4})$$

where $C_2^L(t)$ is defined in eq 25 and

$$C_2^Q(t) = \frac{1}{2}\beta^2\langle \delta A^2(t)(\delta\Delta V(0))^2 \rangle \quad (\text{A.5})$$

In eq A.4, the last three terms are the second-order corrections to the LR expression in eq 27, and if $\delta\Delta V(0)$, $\delta A(t)$, $\delta A^2(t)$ follow Gaussian distributions, $C_1^Q(t)$ and $C_2^Q(t)$ should vanish, which can be used to test if Gaussian statistics assumption is satisfied. Figure 6 shows the comparison between NLR, LR, QR results in the case of $\pi\pi^* \rightarrow \text{CT1}$ transition in the bent triad. It is noted that the second-order terms lead to rather small effects to the overall IMT time-dependent quantities, i.e. \bar{U}_t and σ_t^2 , and thus QR agrees with LR predictions for IMT rates.

■ AUTHOR INFORMATION

Corresponding Author

Xiang Sun – Division of Arts and Sciences, NYU Shanghai, Shanghai 200122, China; NYU-ECNU Center for Computational Chemistry at NYU Shanghai, Shanghai 200062, China; Department of Chemistry, New York University, New York 10003, United States;  orcid.org/0000-0002-2846-8532; Email: xiang.sun@nyu.edu

Author

Dominikus Brian – Division of Arts and Sciences, NYU Shanghai, Shanghai 200122, China; NYU-ECNU Center for Computational Chemistry at NYU Shanghai, Shanghai 200062, China; Department of Chemistry, New York University, New York 10003, United States;  orcid.org/0000-0001-6165-0355

Complete contact information is available at:
<https://pubs.acs.org/10.1021/acs.jctc.0c01250>

Notes

The authors declare no competing financial interest.

ACKNOWLEDGMENTS

We would like to thank Eitan Geva, Barry Dunietz, and Margaret Cheung for intriguing discussions. X.S. acknowledges support from NYU Shanghai, the National Natural Science Foundation of China (No. 21903054), Shanghai Sailing Program (No. 19YF1435600), and the Program for Eastern Young Scholar at Shanghai Institutions of Higher Learning. Computing resources were provided by NYU Shanghai HPC.

REFERENCES

- (1) Park, S.; Steen, C. J.; Lyska, D.; Fischer, A. L.; Endelman, B.; Iwai, M.; Niyogi, K. K.; Fleming, G. R. Chlorophyll-Carotenoid Excitation Energy Transfer and Charge Transfer in *Nannochloropsis Oceanica* for the Regulation of Photosynthesis. *Proc. Natl. Acad. Sci. U. S. A.* **2019**, *116*, 3385–3390.
- (2) Zhang, J. Z.; Reisner, E. Advancing Photosystem II Photoelectrochemistry for Semi-Artificial Photosynthesis. *Nat. Rev. Chem.* **2020**, *4*, 6–21.
- (3) Wasielewski, M. R. Photoinduced Electron Transfer in Supramolecular Systems for Artificial Photosynthesis. *Chem. Rev.* **1992**, *92*, 435–461.
- (4) Romero, E.; Novoderezhkin, V. I.; van Grondelle, R. Quantum Design of Photosynthesis for Bio-Inspired Solar-Energy Conversion. *Nature* **2017**, *543*, 355–365.
- (5) Schuller, J. M.; Birrell, J. A.; Tanaka, H.; Konuma, T.; Wulffhorst, H.; Cox, N.; Schuller, S. K.; Thiemann, J.; Lubitz, W.; Sétil, P.; Ikegami, T.; Engel, B. D.; Kurisu, G.; Nowaczyk, M. M. Structural Adaptations of Photosynthetic Complex I Enable Ferredoxin-Dependent Electron Transfer. *Science* **2019**, *363*, 257–260.
- (6) Proppe, A. H.; Li, Y. C.; Aspuru-Guzik, A.; Berlinguet, C. P.; Chang, C. J.; Cogdell, R.; Doyle, A. G.; Flick, J.; Gabor, N. M.; Grondelle, R.; Hammes-Schiffer, S.; Jaffer, S. A.; Kelley, S. O.; Leclerc, M.; Leo, K.; Mallouk, T. E.; Narang, P.; Schlau-Cohen, G. S.; Scholes, G. D.; Vojvodic, A.; Yam, V. W.-W.; Yang, J. Y.; Sargent, E. H. Bioinspiration in Light Harvesting and Catalysis. *Nat. Rev. Mater.* **2020**, *103*, 1–19.
- (7) Lin, F.; Jiang, K.; Kaminsky, W.; Zhu, Z.; Jen, A. K. A Nonfullerene Acceptor with Enhanced Intermolecular π -Core Interaction for High-Performance Organic Solar Cells. *J. Am. Chem. Soc.* **2020**, *142*, 15246–15251.
- (8) Wang, T.; Brédas, J. L. Organic Solar Cells Based on Nonfullerene Small-Molecule Acceptors: Impact of Substituent Position. *Matter* **2020**, *2*, 119–135.
- (9) Kurpiers, J.; Ferron, T.; Roland, S.; Jakoby, M.; Thiede, T.; Jaiser, F.; Albrecht, S.; Janietz, S.; Collins, B. A.; Howard, I. A.; Neher, D. Probing the Pathways of Free Charge Generation in Organic Bulk Heterojunction Solar Cells. *Nat. Commun.* **2018**, *9*, 2038.
- (10) Han, G.; Guo, Y.; Song, X.; Wang, Y.; Yi, Y. Terminal π - π Stacking Determines Three-Dimensional Molecular Packing and Isotropic Charge Transport in an A- π -A Electron Acceptor for Non-Fullerene Organic Solar Cells. *J. Mater. Chem. C* **2017**, *5*, 4852–4857.
- (11) Zhao, W.; Li, S.; Yao, H.; Zhang, S.; Zhang, Y.; Yang, B.; Hou, J. Molecular Optimization Enables over 13% Efficiency in Organic Solar Cells. *J. Am. Chem. Soc.* **2017**, *139*, 7148–7151.
- (12) Falke, S. M.; Rozzi, C. A.; Brida, D.; Maiuri, M.; Amato, M.; Sommer, E.; De Sio, A.; Rubio, A.; Cerullo, G.; Molinari, E.; Lienau, C. Coherent Ultrafast Charge Transfer in an Organic Photovoltaic Blend. *Science* **2014**, *344*, 1001–1005.
- (13) Bottari, G.; de la Torre, G.; Guldi, D. M.; Torres, T. Covalent and Noncovalent Phthalocyanine-Carbon Nanostructure Systems: Synthesis, Photoinduced Electron Transfer, and Application to Molecular Photovoltaics. *Chem. Rev.* **2010**, *110*, 6768–6816.
- (14) Benatto, L.; Marchiori, C. F.; Talka, T.; Aramini, M.; Yamamoto, N. A.; Huotari, S.; Roman, L. S.; Koehler, M. Comparing C₆₀ and C₇₀ as Acceptor in Organic Solar Cells: Influence of the Electronic Structure and Aggregation Size on the Photovoltaic Characteristics. *Thin Solid Films* **2020**, *697*, 137827.
- (15) Tinnin, J.; Bhandari, S.; Zhang, P.; Aksu, H.; Maiti, B.; Geva, E.; Dunietz, B. D.; Sun, X.; Cheung, M. S. Molecular-Level Exploration of the Structure-Function Relations Underlying Interfacial Charge Transfer in the Subphthalocyanine/C₆₀ Organic Photovoltaic System. *Phys. Rev. Appl.* **2020**, *13*, 054075.
- (16) Lee, M. H.; Dunietz, B. D.; Geva, E. Donor-to-Donor vs Donor-to-Acceptor Interfacial Charge Transfer States in the Phthalocyanine-Fullerene Organic Photovoltaic System. *J. Phys. Chem. Lett.* **2014**, *5*, 3810–3816.
- (17) Zhao, Y.; Liang, W. Charge Transfer in Organic Molecules for Solar Cells: Theoretical Perspective. *Chem. Soc. Rev.* **2012**, *41*, 1075–1087.
- (18) Madsen, N. K.; Hansen, M. B.; Worth, G. A.; Christiansen, O. MR-MCTDH[n]: Flexible Configuration Spaces and Nonadiabatic Dynamics within the MCTDH[n] Framework. *J. Chem. Theory Comput.* **2020**, *16*, 4087–4097.
- (19) Jiang, B.; Li, J.; Guo, H. High-Fidelity Potential Energy Surfaces for Gas-Phase and Gas-Surface Scattering Processes from Machine Learning. *J. Phys. Chem. Lett.* **2020**, *11*, 5120–5131.
- (20) Beyer, A. N.; Richardson, J. O.; Knowles, P. J.; Rommel, J.; Althorpe, S. C. Quantum Tunneling Rates of Gas-Phase Reactions from On-the-Fly Instanton Calculations. *J. Phys. Chem. Lett.* **2016**, *7*, 4374–4379.
- (21) Crespo-Otero, R.; Barbatti, M. Recent Advances and Perspectives on Nonadiabatic Mixed Quantum-Classical Dynamics. *Chem. Rev.* **2017**, *107*, 7026–7068.
- (22) Chen, W.-K.; Liu, X.-Y.; Fang, W.-H.; Dral, P. O.; Cui, G. Deep Learning for Nonadiabatic Excited-State Dynamics. *J. Phys. Chem. Lett.* **2018**, *9*, 6702–6708.
- (23) Wehrle, M.; Oberli, S.; Vaníček, J. On-the-Fly Ab Initio Semiclassical Dynamics of Floppy Molecules: Absorption and Photoelectron Spectra of Ammonia. *J. Phys. Chem. A* **2015**, *119*, 5685–5690.
- (24) Marcus, R. A. On the Theory of Oxidation-Reduction Reactions Involving Electron Transfer. I. *J. Chem. Phys.* **1956**, *24*, 966–978.
- (25) Marcus, R. A. Electrostatic Free Energy and Other Properties of States Having Nonequilibrium Polarization. I. *J. Chem. Phys.* **1956**, *24*, 979–989.
- (26) Marcus, R. A. Electron Transfer Reactions in Chemistry. Theory and Experiment. *Rev. Mod. Phys.* **1993**, *65*, 599.
- (27) Sun, X.; Geva, E. Equilibrium Fermi's Golden Rule Charge Transfer Rate Constants in the Condensed Phase: The Linearized Semiclassical Method vs Classical Marcus Theory. *J. Phys. Chem. A* **2016**, *120*, 2976–2990.
- (28) Coalson, R. D.; Evans, D. G.; Nitzan, A. A Nonequilibrium Golden Rule Formula for Electronic State Populations in Nonadiabatically Coupled Systems. *J. Chem. Phys.* **1994**, *101*, 436–44.
- (29) Cho, M.; Silbey, R. J. Nonequilibrium Photoinduced Electron Transfer. *J. Chem. Phys.* **1995**, *103*, 595–606.
- (30) Izmaylov, A. F.; Mendive Tapia, D.; Bearpark, M. J.; Robb, M. A.; Tully, J. C.; Frisch, M. J. Nonequilibrium Fermi Golden Rule for Electronic Transitions Through Conical Intersections. *J. Chem. Phys.* **2011**, *135*, 234106–15.
- (31) Sun, X.; Geva, E. Nonequilibrium Fermi's Golden Rule Charge Transfer Rates via the Linearized Semiclassical Method. *J. Chem. Theory Comput.* **2016**, *12*, 2926–2941.
- (32) Hu, Z.; Tong, Z.; Cheung, M. S.; Dunietz, B. D.; Geva, E.; Sun, X. Photoinduced Charge Transfer Dynamics in the Carotenoid-Porphyrin-C₆₀ Triad via the Linearized Semiclassical Nonequilibrium Fermi's Golden Rule. *J. Phys. Chem. B* **2020**, *124*, 9579–9591.

- (33) Sun, X.; Geva, E. Non-Condon Nonequilibrium Fermi's Golden Rule Rates from the Linearized Semiclassical Method. *J. Chem. Phys.* **2016**, *145*, 064109.
- (34) Liddell, P. A.; Kuciauskas, D.; Sumida, J. P.; Nash, B.; Nguyen, D.; Moore, A. L.; Moore, T. A.; Gust, D. Photoinduced Charge Separation and Charge Recombination to a Triplet State in a Carotene-Porphyrin-Fullerene Triad. *J. Am. Chem. Soc.* **1997**, *119*, 1400–1405.
- (35) Carbonera, D.; Di Valentin, M.; Corvaja, C.; Agostini, G.; Giacometti, G.; Liddell, P. A.; Kuciauskas, D.; Moore, A. L.; Moore, T. A.; Gust, D. EPR Investigation of Photoinduced Radical Pair Formation and Decay to a Triple State in a Carotene-Porphyrin-Fullerene Triad. *J. Am. Chem. Soc.* **1998**, *120*, 4398–4405.
- (36) Kuciauskas, D.; Liddell, P. A.; Lin, S.; Stone, S. G.; Moore, A. L.; Moore, T. A.; Gust, D. Photoinduced Electron Transfer in Carotenoporphyrin-Fullerene Triads: Temperature and Solvent Effects. *J. Phys. Chem. B* **2000**, *104*, 4307–4321.
- (37) Gust, D.; Moore, T. A.; Moore, A. L. Mimicking Photosynthetic Solar Energy Transduction. *Acc. Chem. Res.* **2001**, *34*, 40–48.
- (38) Spallanzani, N.; Rozzi, C. A.; Varsano, D.; Baruah, T.; Pederson, M. R.; Manghi, F.; Rubio, A. Photoexcitation of a Light-Harvesting Supramolecular Triad: A Time-Dependent DFT Study. *J. Phys. Chem. B* **2009**, *113*, 5345–5349.
- (39) Andrea Rozzi, C.; Maria Falke, S.; Spallanzani, N.; Rubio, A.; Molinari, E.; Brida, D.; Maiuri, M.; Cerullo, G.; Schramm, H.; Christoffers, J.; Lienau, C. Quantum Coherence Controls the Charge Separation in a Prototypical Artificial Light-Harvesting System. *Nat. Commun.* **2013**, *4*, 1602–1607.
- (40) Su, G.; Czader, A.; Homouz, D.; Bernardes, G.; Mateen, S.; Cheung, M. S. Multiscale Simulation on a Light-Harvesting Molecular Triad. *J. Phys. Chem. B* **2012**, *116*, 8460–8473.
- (41) Balamurugan, D.; Aquino, A. J. A.; de Dios, F.; Flores, L., Jr.; Lischka, H.; Cheung, M. S. Multiscale Simulation of the Ground and Photo-Induced Charge-Separated States of a Molecular Triad in Polar Organic Solvent: Exploring the Conformations, Fluctuations, and Free Energy Landscapes. *J. Phys. Chem. B* **2013**, *117*, 12065–12075.
- (42) Manna, A. K.; Balamurugan, D.; Cheung, M. S.; Dunietz, B. D. Unraveling the Mechanism of Photoinduced Charge Transfer in Carotenoid-Porphyrin-C₆₀ Molecular Triad. *J. Phys. Chem. Lett.* **2015**, *6*, 1231–1237.
- (43) Starovoytov, O. N.; Zhang, P.; Cieplak, P.; Cheung, M. S. Induced Polarization Restricts the Conformational Distribution of a Light-Harvesting Molecular Triad in the Ground State. *Phys. Chem. Chem. Phys.* **2017**, *19*, 22969–22980.
- (44) Sun, X.; Zhang, P.; Lai, Y.; Williams, K. L.; Cheung, M. S.; Dunietz, B. D.; Geva, E. Computational Study of Charge-Transfer Dynamics in the Carotenoid-Porphyrin-C₆₀ Molecular Triad Solvated in Explicit Tetrahydrofuran and Its Spectroscopic Signature. *J. Phys. Chem. C* **2018**, *122*, 11288–11299.
- (45) Stratt, R. M.; Maroncelli, M. Nonreactive Dynamics in Solution: The Emerging Molecular View of Solvation Dynamics and Vibrational Relaxation. *J. Phys. Chem.* **1996**, *100*, 12981–12996.
- (46) Chandler, D. *Introduction to Modern Statistical Mechanics*; Oxford University Press: New York, 1987; Chapter 8.
- (47) Zwanzig, R. *Nonequilibrium Statistical Mechanics*; Oxford University Press: New York, 2001; Chapter 7.
- (48) Carter, E. A.; Hynes, J. T. Solute-Dependent Solvent Force Constants for Ion Pairs and Neutral Pairs in a Polar Solvent. *J. Phys. Chem.* **1989**, *93*, 2184–2187.
- (49) Carter, E. A.; Hynes, J. T. Solvation Dynamics for an Ion Pair in a Polar Solvent: Time-Dependent Fluorescence and Photochemical Charge Transfer. *J. Chem. Phys.* **1991**, *94*, 5961–5979.
- (50) Georgievskii, Y.; Hsu, C. P.; Marcus, R. A. Linear Response in Theory of Electron Transfer Reactions as an Alternative to the Molecular Harmonic Oscillator Model. *J. Chem. Phys.* **1999**, *110*, 5307–5317.
- (51) Bragg, A. E.; Cavanagh, M. C.; Schwartz, B. J. Linear Response Breakdown in Solvation Dynamics Induced by Atomic Electron-Transfer Reactions. *Science* **2008**, *321*, 1817–1822.
- (52) Moskun, A. C.; Jailaubekov, A. E.; Bradford, S. E.; Tao, G. H.; Stratt, R. M. Rotational Coherence and a Sudden Breakdown in Linear Response Seen in Room-Temperature Liquids. *Science* **2006**, *311*, 1907–1911.
- (53) Tao, G.; Stratt, R. M. The Molecular Origins of Nonlinear Response in Solute Energy Relaxation: The Example of High-Energy Rotational Relaxation. *J. Chem. Phys.* **2006**, *125*, 114501–18.
- (54) Turi, L.; Minář, P.; Rossky, P. J. Non-linear Response and Hydrogen Bond Dynamics for Electron Solvation in Methanol. *Chem. Phys. Lett.* **2000**, *316*, 465–470.
- (55) Fonseca, T.; Ladanyi, B. M. Breakdown of Linear Response for Solvation Dynamics in Methanol. *J. Phys. Chem.* **1991**, *95*, 2116–2119.
- (56) Maroncelli, M.; Fleming, G. R. Computer Simulation of the Dynamics of Aqueous Solvation. *J. Chem. Phys.* **1988**, *89*, 5044–5069.
- (57) Heid, E.; Schröder, C. Solvation Dynamics in Polar Solvents and Imidazolium Ionic Liquids: Failure of Linear Response Approximations. *Phys. Chem. Chem. Phys.* **2018**, *20*, 5246–5255.
- (58) Hazra, M. K.; Bagchi, B. Non-Linearity in Dipolar Solvation Dynamics in Water-Ethanol Mixture: Composition Dependence of Free Energy Landscape. *J. Chem. Phys.* **2019**, *151*, 084502.
- (59) Geissler, P. L.; Chandler, D. Importance Sampling and Theory of Nonequilibrium Solvation Dynamics in Water. *J. Chem. Phys.* **2000**, *113*, 9759–9765.
- (60) Simonson, T. Gaussian Fluctuations and Linear Response in an Electron Transfer Protein. *Proc. Natl. Acad. Sci. U. S. A.* **2002**, *99*, 6544–6549.
- (61) Laird, B. B.; Thompson, W. H. On the Connection Between Gaussian Statistics and Excited-State Linear Response for Time-Dependent Fluorescence. *J. Chem. Phys.* **2007**, *126*, 211104.
- (62) Laird, B. B.; Thompson, W. H. Time-Dependent Fluorescence in Nanoconfined Solvents: Linear-response Approximations and Gaussian Statistics. *J. Chem. Phys.* **2011**, *135*, 084511.
- (63) Furse, K. E.; Corcelli, S. A. Molecular Dynamics Simulations of DNA Solvation Dynamics. *J. Phys. Chem. Lett.* **2010**, *1*, 1813–1820.
- (64) Nilsson, L.; Halle, B. Molecular Origin of Time-Dependent Fluorescence Shifts in Proteins. *Proc. Natl. Acad. Sci. U. S. A.* **2005**, *102*, 13867–13872.
- (65) Sun, X. Hybrid Equilibrium-Nonequilibrium Molecular Dynamics Approach for Two-Dimensional Solute-Pump/Solvent-Probe Spectroscopy. *J. Chem. Phys.* **2019**, *151*, 194507.
- (66) Sun, X.; Ladanyi, B. M.; Stratt, R. M. Effects of Electronic-State-Dependent Solute Polarizability: Application to Solute-Pump/Solvent-Probe Spectra. *J. Phys. Chem. B* **2015**, *119*, 9129–9139.
- (67) Sun, X.; Stratt, R. M. How a Solute-Pump/Solvent-Probe Spectroscopy Can Reveal Structural Dynamics: Polarizability Response Spectra as a Two-Dimensional Solvation Spectroscopy. *J. Chem. Phys.* **2013**, *139*, 044506.
- (68) Sun, X.; Stratt, R. M. The Molecular Underpinnings of a Solute-Pump/Solvent-Probe Spectroscopy: The Theory of Polarizability Response Spectra and an Application to Preferential Solvation. *Phys. Chem. Chem. Phys.* **2012**, *14*, 6320–6331.
- (69) Dunbar, J. A.; Arthur, E. J.; White, A. M.; Kubarych, K. J. Ultrafast 2D-IR and Simulation Investigations of Preferential Solvation and Cosolvent Exchange Dynamics. *J. Phys. Chem. B* **2015**, *119*, 6271–6279.
- (70) Tong, Z.; Gao, X.; Cheung, M. S.; Dunietz, B. D.; Geva, E.; Sun, X. Charge Transfer Rate Constants for the Carotenoid-Porphyrin-C₆₀ Molecular Triad Dissolved in Tetrahydrofuran: The Spin-Boson Model vs the Linearized Semiclassical Approximation. *J. Chem. Phys.* **2020**, *153*, 044105.
- (71) Chandler, D. *Introduction to Modern Statistical Mechanics*; Oxford University Press: New York, 1987.
- (72) Tuckerman, M. E. *Statistical Mechanics: Theory and Molecular Simulation*; Oxford University Press: New York, 2010.

- (73) Nitzan, A. *Chemical Dynamics in Condensed Phases: Relaxation, Transfer and Reactions in Condensed Molecular Systems*; Oxford University Press, 2006.
- (74) Zwanzig, R. *Nonequilibrium Statistical Mechanics*; Oxford University Press: New York, 2001.
- (75) Wick, G. C. The Evaluation of the Collision Matrix. *Phys. Rev.* **1950**, *80*, 268–272.
- (76) Baer, R.; Neuhauser, D. Density Functional Theory with Correct Long-Range Asymptotic Behavior. *Phys. Rev. Lett.* **2005**, *94*, 043002.
- (77) Livshits, E.; Baer, R. A Well-Tempered Density Functional Theory of Electrons in Molecules. *Phys. Chem. Chem. Phys.* **2007**, *9*, 2932–2941.
- (78) Stein, T.; Eisenberg, H.; Kronik, L.; Baer, R. Fundamental Gaps in Finite Systems from Eigenvalues of a Generalized Kohn-Sham Method. *Phys. Rev. Lett.* **2010**, *105*, 266802.
- (79) Voityuk, A. A.; Rösch, N. Fragment Charge Difference Method for Estimating Donor-Acceptor Electronic Coupling: Application to DNA π -Stacks. *J. Chem. Phys.* **2002**, *117*, 5607–5616.
- (80) Case, D. A.; Ben-Shalom, I. Y.; Brozell, S. R.; Cerutti, D. S.; Cheatham, III, T. E.; Cruzeiro, V. W. D.; Darden, T. A.; Duke, R. E.; Ghoreishi, D.; Gilson, M. K.; Gohlke, H.; Goetz, A. W.; et al. *AMBER 2018*; University of California, San Francisco, 2018.
- (81) Darden, T.; York, D.; Pedersen, L. Particle Mesh Ewald: An Nlog(N) Method for Ewald Sums in Large Systems. *J. Chem. Phys.* **1993**, *98*, 10089–10092.
- (82) Ciccotti, G.; Ryckaert, J. P. Molecular Dynamics Simulation of Rigid Molecules. *Comput. Phys. Rep.* **1986**, *4*, 346–392.
- (83) Wang, T.; Su, X.; Zhang, X.; Nie, X.; Huang, L.; Zhang, X.; Sun, X.; Luo, Y.; Zhang, G. Aggregation-Induced Dual-Phosphorescence from Organic Molecules for Nondoped Light-Emitting Diodes. *Adv. Mater.* **2019**, *31*, 1904273–7.
- (84) Wang, T.; Su, X.; Zhang, X.; Huang, W.; Huang, L.; Zhang, X.; Sun, X.; Luo, Y.; Zhang, G. A Combinatory Approach Towards the Design of Organic Polymer Luminescent Materials. *J. Mater. Chem. C* **2019**, *7*, 9917–9925.
- (85) Kovacs, D.; Mathieu, E.; Kiraev, S. R.; Wells, J. A. L.; Demeyere, E.; Sipos, A.; Borbas, K. E. Coordination Environment-Controlled Photoinduced Electron Transfer Quenching in Luminescent Europium Complexes. *J. Am. Chem. Soc.* **2020**, *142*, 13190–13200.
- (86) Pantazis, A.; Westerberg, K.; Althoff, T.; Abramson, J.; Olcese, R. Harnessing Photoinduced Electron Transfer to Optically Determine Protein Sub-nanoscale Atomic Distances. *Nat. Commun.* **2018**, *9*, 4738.
- (87) Polizzi, N. F.; Eibling, M. J.; Perez-Aguilar, J. M.; Rawson, J.; Lanci, C. J.; Fry, H. C.; Beratan, D. N.; Saven, J. G.; Therien, M. J. Photoinduced Electron Transfer Elicits a Change in the Static Dielectric Constant of a *de Novo* Designed Protein. *J. Am. Chem. Soc.* **2016**, *138*, 2130–2133.